Contents lists available at ScienceDirect

Biomaterials

journal homepage: www.elsevier.com/locate/biomaterials

In vitro and in vivo evaluation of biohybrid tissue-engineered vascular grafts with transformative ^{1}H/^{19}F MRI traceable scaffolds

Elena Rama [a], Saurav Ranjan Mohapatra [b], Yukiharu Sugimura [c], Tomoyuki Suzuki [c], Stefan Siebert [b], Roman Barmin [a], Juliane Hermann [d], Jasmin Baier [a], Anne Rix [a], Teresa Lemainque [a,e], Susanne Koletnik [a], Asmaa Said Elshafei [a], Roger Molto Pallares [a], Seyed Mohammadali Dadfar [a,f], René H. Tolba [g], Volkmar Schulz [a], Joachim Jankowski [d,h,i], Christian Apel [b], Payam Akhyari [c], Stefan Jockenhoevel [b], Fabian Kiessling [a,*]

[a] *Institute for Experimental Molecular Imaging, Faculty of Medicine, RWTH Aachen University, Forckenbeckstraße 55, 52074 Aachen, Germany*
[b] *Department of Biohybrid & Medical Textiles, AME-Institute of Applied Medical Engineering, Helmholtz Institute, RWTH Aachen University, Forckenbeckstraße 55, 52074 Aachen, Germany*
[c] *Department of Cardiac Surgery, Medical Faculty and RWTH University Hospital Aachen, RWTH Aachen University, Aachen, Germany*
[d] *Institute for Molecular Cardiovascular Research (IMCAR), University Hospital RWTH Aachen, Aachen, Germany*
[e] *Department of Diagnostic and Interventional Radiology, Medical Faculty, RWTH Aachen University, 52074 Aachen, Germany*
[f] *Ardena Oss, 5349 AB Oss, the Netherlands*
[g] *Institute for Laboratory Animal Science and Experimental Surgery, Medical Faculty, RWTH Aachen International University, Aachen, Germany*
[h] *Aachen-Maastricht Institute for CardioRenal Disease (AMICARE), University Hospital RWTH Aachen, Aachen, Germany*
[i] *Department of Pathology, Cardiovascular Research Institute Maastricht (CARIM), University of Maastricht, the Netherlands*

ARTICLE INFO

ABSTRACT

Biohybrid tissue-engineered vascular grafts (TEVGs) promise long-term durability due to their ability to adapt to hosts' needs. However, the latter calls for sensitive non-invasive imaging approaches to longitudinally monitor their functionality, integrity, and positioning. Here, we present an imaging approach comprising the labeling of non-degradable and degradable TEVGs' components for their in vitro and in vivo monitoring by hybrid ^{1}H/^{19}F MRI. TEVGs (inner diameter 1.5 mm) consisted of biodegradable poly(lactic-*co*-glycolic acid) (PLGA) fibers passively incorporating superparamagnetic iron oxide nanoparticles (SPIONs), non-degradable polyvinylidene fluoride scaffolds labeled with highly fluorinated thermoplastic polyurethane (^{19}F-TPU) fibers, a smooth muscle cells containing fibrin blend, and endothelial cells. ^{1}H/^{19}F MRI of TEVGs in bioreactors, and after subcutaneous and infrarenal implantation in rats, revealed that PLGA degradation could be faithfully monitored by the decreasing SPIONs signal. The ^{19}F signal of ^{19}F-TPU remained constant over weeks. PLGA degradation was compensated by cells' collagen and α-smooth-muscle-actin deposition. Interestingly, only TEVGs implanted on the abdominal aorta contained elastin. XTT and histology proved that our imaging markers did not influence extracellular matrix deposition and host immune reaction. This concept of non-invasive longitudinal assessment of cardiovascular implants using ^{1}H/^{19}F MRI might be applicable to various biohybrid tissue-engineered implants, facilitating their clinical translation.

1. Introduction

Cardiovascular diseases (CVD), such as deep vein thrombosis, aortic, coronary artery, cerebrovascular, and peripheral artery disease, combined with longstanding diabetes and hypertension, as well as an ever-increasing aging population, are the leading cause of death worldwide [1,2]. Common surgical strategies for treating CVD include coronary artery bypass or major arterial reconstruction. Bypassing obstructed or aneurysmal vascular segments through an autologous graft, such as saphenous vein, radial, and mammary artery, is currently the preferred clinical treatment [3]. It does not trigger an immune foreign body reaction, preventing graft rejection, and already possesses a functional

endothelial layer that prevents thrombosis or excessive smooth muscle cell (SMC) proliferation. However, autologous grafts present a substantial drawback, namely donor morbidity that prevents autografting [4].

Synthetic grafts, e.g., from expanded polytetrafluoroethylene (GORE-TEX), poly(ethylene terephthalate) (Dacron), and polyurethane (PU), are viable alternatives [5]. Currently, synthetic grafts dominate the global vascular grafts market with an estimated compound annual growth rate (CAGR) of 7.0 % from 2022 to 2030 (source: Grand View Research, Report ID: 978-1-68038-628-8). Despite their extensive use in standard clinical practice, synthetic grafts have many limitations as they tend to exacerbate chronic immune reactions, inflammation, calcification, thrombosis, and stenosis parallel to their inability to grow with the host organism, lack of remodeling, compliance mismatch, and limited application to >6 mm diameter blood vessels [6,7].

As a future alternative, biohybrid tissue-engineered vascular grafts (TEVGs) are being developed [8,9]. Their scaffolds often combine non-degradable and biodegradable materials to optimally balance scaffold durability and adaptability. Indeed, the presence of a permanent scaffold, albeit minimal, is needed to withstand blood pressure during in vivo implantation and ensure graft integrity, while the presence of biodegradable materials is needed to facilitate scaffold growth, remodeling, and integration within the host organism. Notably, the degradation of these biodegradable materials induces mechanical stress, which in turn triggers extracellular matrix (ECM) production, thereby preserving the structural integrity of the graft and facilitating the restoration of native-like tissue. Additionally, this process allows for scaffold reshaping, preventing the formation of a too-rigid structure that could hinder the physiological integration and maturation of TEVGs. However, the production of native-like ECM is not always guaranteed since it depends on several interconnected mechano- and immune-driven processes. Key factors such as scaffold topography (pore and fiber size), scaffold chemical composition, and material degradation rate influence and are influenced by the ECM-cell interaction, matrix-bound vesicles-mediated ECM immunomodulatory effects, as well as integrin-mediated cell response, infiltration rate of T-cells and M2 macrophages [8,9]. The latter are fundamental for a functional endothelium, SMCs proliferation, and consequent release of pro-inflammatory cytokines and anti-inflammatory cytokines, i.e., IL-10 responsible for ECM remodeling via matrix metalloproteinase-9.

Due to the high flexibility of TEVGs to adapt to their environment, dysregulation and dysfunction may already occur during in vitro maturation as well as during the in vivo remodeling. Thus, regular monitoring of TEVGs' in vitro and in vivo maturation is mandatory to e. g., avoid the implantation of dysfunctional systems, and early detect and treat rejection, acute/chronic inflammation, as well as loss of graft patency due to thrombosis and stenosis [10–13].

In this context, magnetic resonance imaging (MRI) is one of the most powerful diagnostic tools. Despite the higher costs and longer processing times associated with MRI compared to other routinely employed imaging techniques (i.e., X-ray fluoroscopy and computed tomography), MRI offers a better soft tissue contrast and provides complementary functional information. Even though it is worth noting that CT technology is currently strongly evolving towards higher sensitivity and specificity due to the introduction of single photon counting and spectral detectors, MRI further advantages are the lack of ionizing radiation, and the higher sensitivity imaging markers (micromolar range in comparison to millimolar range in CT) [14,15]. Many ^{1}H contrast agents are (pre)clinically employed, e.g., gadolinium (Gd)- or iron-based (i.e., superparamagnetic iron oxide nanoparticles, SPIONs), to acquire distinct tissue characteristics [16,17]. However, to enhance the specificity for material detection, several studies headed their research toward the application of ^{19}F MRI as a parallel alternative to ^{1}H MRI [18]. The almost complete lack of endogenous ^{19}F in the human body leads to an almost linear relationship between ^{19}F content and measured signal [19,20]. Nevertheless, due to the limited signal sensitivity of current MR

hardware (in the range of mM concentrations) and the low abundance of ^{19}F nuclei in vivo following exogenous administration, high concentrations of mobile ^{19}F equivalent atoms are required. Commonly used fluoropolymers, such as polyvinylidene fluoride (PVDF), polytetrafluoroethylene (PTFE), perfluoroalkoxy (PFA), fluorinated ethylene propylene (FEP), ethylene tetrafluoroethylene (ETFE), and ethylene chlorotrifluoroethylene (ECTFE), exhibit excellent characteristics for tissue engineering purposes. However, they are entirely unsuitable for ^{19}F MRI applications given their high crystallinity, which results in a rapid decay of the MRI signal for mechanically rigid ^{19}F atoms. Previous studies addressed this limitation by utilizing a novel highly fluorinated polymer, fluorinated thermoplastic polyurethane (^{19}F-TPU), which possesses an amorphous structure and a large number of magnetically equivalent ^{19}F atoms capable to vibrate freely [21,22]. ^{19}F-TPU differs from other MRI markers i.e., Gadolinium, which are detected through a change in relaxivity based on the chemical environment. Moreover, ^{19}F-TPU offers several advantages, including biocompatibility, chemical inertness, and non-immunogenicity.

To ensure non-invasive monitoring of TEVGs' remodeling without losing track of their positioning and structural integrity, we here propose the combined use of permanent fibers (^{19}F-TPU and PVDF) and a biodegradable component, poly(lactic-*co*-glycolic acid) (PLGA). This FDA-approved biodegradable polymer is known for its versatility, strong physical properties, high biocompatibility, tuneable physical properties, non-toxic degradation by-products, extensive research support, and clinical experience [23]. As shown in Fig. 1, we first incorporated oleic acid coated SPIONs into the core of the PLGA fibers and added ^{19}F-TPU to the main PVDF tubular scaffold to compensate for their lack of MR visibility and monitorability. TEVGs were finally obtained by molding the textile scaffold with fibrin gel containing SMCs and endothelial cells (ECs). The incorporation of the selected MRI labels (SPIONs and ^{19}F) ensured the non-invasive longitudinal monitoring of TEVGs via hybrid ^{1}H/^{19}F MRI. This allowed efficient assessment of SPIONs-labeled PLGA fibers (SPION-PLGA) degradation over time and permanent monitoring of the positioning and integrity of the TEVGs both in vitro during bioreactor conditioning and in vivo as subcutaneous implants as well as abdominal aorta bypass in rats. Moreover, the excellent biocompatibility of all textile components used in our model of TEVGs was thoroughly investigated via cytotoxicity assays and histological analyses.

2. Materials and methods

2.1. Textile scaffold production

2.1.1. PVDF mesh
PVDF (Lenzing Plastics GmbH & co. KG, Lenzing, Austria) multifilament fibers (150 dtex, 48 filaments) were employed to produce a tubular textile scaffold using a double-bar raschel warp-knitting machine (RIUS, COMATEX, Barcelona, Spain).

2.1.2. Oleic acid-coated SPIONs
Oleic acid-coated SPIONs were synthesized by thermal decomposition based on a previously established protocol [24,25]. Briefly, 7.2 g of the iron (III) oleate and 18.4 g of oleic acid were dissolved in 50 mL of 1-octadecene. Then, the mixture was heated to 100 °C and maintained at this temperature without reflux for 30 min. After degassing, fitting a reflux cooler, and purging the flask with argon, the reaction mixture was heated further to 340 °C with a heating rate of 3 °C min^{-1} under argon atmosphere for 3 h. After cooling down to room temperature, the freshly prepared nanoparticles were precipitated by adding acetone to the flask. The mixture was sonicated, centrifuged and the supernatant was discarded. Finally, the washed nanoparticles were dispersed in hexane and methanol (1:6) and further centrifuged. Following several washing steps, one drop of oleic acid was added to the nanoparticles dispersed in hexane.
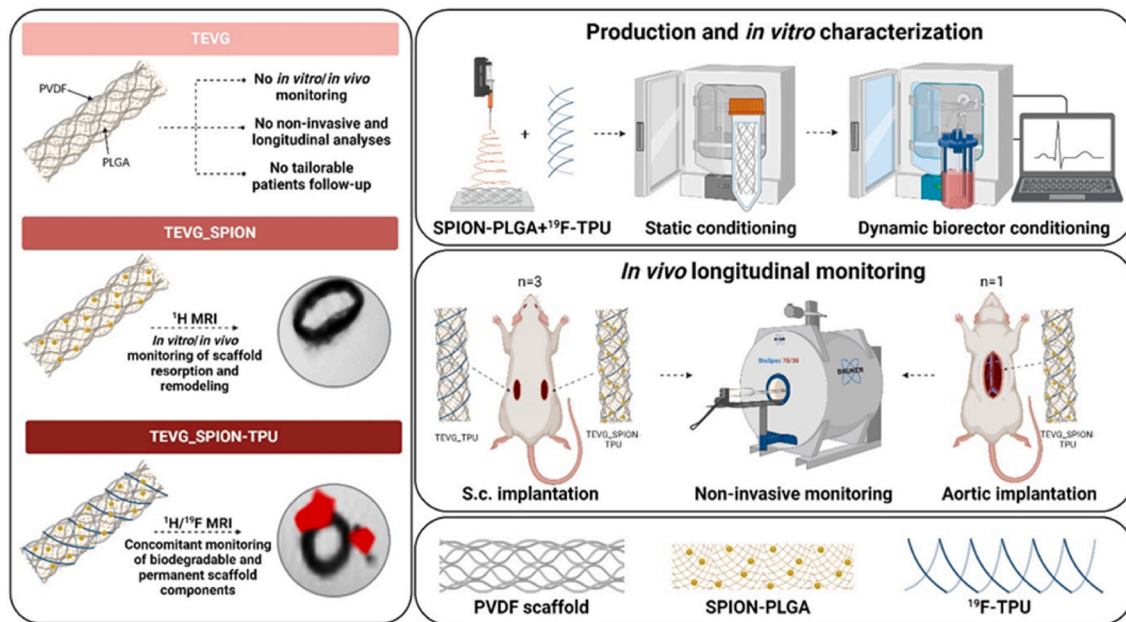
Fig. 1. Schematic depiction of the study design (Created with BioRender.com).

2.1.3. Electrospun SPION-PLGA fibers

As described in a previously published protocol, a coaxial spinning head (Bioinicia SL, Paterna, Spain) with two coaxial arranged steel capillaries with inner diameters of 1400 μm (shell capillary) and 580 μm (core capillary) were used [12]. To obtain a core-shell fiber structure, a solution containing 6 % (w/w) PLGA labeled with 0.2 % (w/w) SPIONs was used for the core and one with 6 % (w/w) PLGA was employed for the shell. The SPION-PLGA fibers were spun at a voltage of +22 kV (emitter) and −20 kV (collector) at 25 °C and 30 % humidity. Both spinning solutions were prepared by dissolving the PLGA in methanol and chloroform (MeOH, neoLab Migge Laborbedarf – Vertriebs GmbH, Heidelberg, Germany and CHCl3, Carl Roth GmbH & Co. KG, Karlsruhe, Germany). SPIONs were added to the core solution shortly before starting the electrospinning procedure. After placing the PVDF warp-knitted scaffold on a cylindrical collector, the spinning head, placed at a distance of 15 cm, was moved over the entire length of the meshes at a speed of 30 mm s^{-1} with core and shell solutions' flow rates set to 0.5 mL h^{-1} and 1 mL h^{-1}.

2.1.4. ^{19}F-TPU fibers

^{19}F-TPU was purchased as granules from Lubrizol, Wickliffe, Ohio, United States, and dried at 80 °C for 24 h prior to spinning. To obtain multifilaments (68 dtex, 48 filaments) via melt spinning (Fourné Polymertechnik GmbH, Alfter, Germany), a blow chamber, multifilament spinnerets, heating godet and a winder were used with process temperatures ranging from 185 to 220 °C.

2.2. TEVGs preparation

2.2.1. Harvesting of syngeneic cells

All animal experiments were approved by the German State Office for Nature, Environment and Consumer Protection (LANUV) North Rhine-Westphalia and performed in adherence to institutional guidelines, EU Directive 2010/63, and the German federal law on the protection of animals. All animals received humane care conforming to the principles of the "Guide for the Care and Use of Laboratory Animals" (8th Edition, National Institutes of Health (NIH) Publication, 2011, USA). The study was designed, executed, and reported in line with the "Animal Research: Reporting of In Vivo Experiments" (ARRIVE) guidelines. Inbred Lewis male rats (Strain name: LEW/OrlRj, Janvier Labs, Le Genest Saint Isle, France) were chosen as the appropriate animal model.

Inbred siblings share nearly identical genetic pools, allowing TEVGs containing cells harvested from one sibling to be implanted in another without causing inflammation or graft rejection. Furthermore, euthanizing one donor animal enables the collection of a maximum of cells and tissues, preventing the over-stressing of a single animal with both surgeries - cell and tissue harvesting followed by TEVG implantation. With a ratio of 1:3, cells harvested from one donor animal were used to produce 3 syngeneic TEVGs. ECs were derived from enzymatic digestion of the abdominal aorta, while adipose mesenchymal stem cells were derived from adipose tissue, an easily accessible source that provides a high yield of these cells. These cells display a smooth muscle-like phenotype after in vitro mechanostimulation in the bioreactor [26,27].

2.2.2. Harvesting of human cells

The use of human samples was conducted in compliance with the Ethical Committee approval (EK 2067). Human umbilical cords were used to harvest human umbilical artery smooth muscle cells (HUASMCs) and human umbilical artery endothelial cells (HUAECs).

2.2.3. Bioreactor conditioning of TEVGs

TEVGs for in vitro testing were produced using human cells, while TEVGs intended for implantation into rats were produced using syngeneic cells from Lewis male rats. In detail, a silicon tube of 2.4 mm inner diameter (Carl Roth GmbH, Germany) and a metal rod of 1.5 mm diameter were used for the molding of the textile scaffold. As described in a previously published protocol, TEVGs containing human cells were produced using 10 mg mL^{-1} fibrinogen (Calbiochem, Darmstadt, Germany), 40 U mL^{-1} thrombin (Sigma, Steinheim, Germany), TRIS buffer, and 50 mM CaCl₂ (Sigma, Steinheim, Germany), and 10 × 10^6 HUASMCs mL^{-1} and a total of 1.4 mL per cm graft were injected into the silicon tube containing the textile scaffold and the metal rod [12]. 3 × 10^6 HUAECs mL^{-1} and a total of 1 mL per cm graft were employed for the endothelialization of the TEVGs lumen, which was performed under constant rotation for 24 h. TEVGs underwent bioreactor conditioning for a maximum of 4–7 days.

For all TEVGs, the employed bioreactor system consisted of i) a 500 mL medium reservoir, ii) a peristaltic pump (MCP Process, Ismatec, Cole Parmer GmbH, Germany) to modulate the medium dynamic flow, and iii) flow and pressure sensors (Em-tec GmbH, Finning, Germany and Codan GmbH, Lensahn, Germany) to monitor flow and pressure within the system.

The mechanical properties of our TEVGs were assessed, focusing on burst, biaxial, and suture retention strength, as described in a previously published protocol [22]. All tested parameters demonstrated that our TEVGs are characterized by sufficient mechanical strength. The presence of ^{19}F-TPU fibers sutured on the preexisting PVDF and PLGA textile scaffold are expected to not affect the prostheses' mechanical properties.

2.3. MRI longitudinal evaluation of SPION-PLGA fiber degradation

A Bruker BioSpec 70/20 USR 7 T MRI scanner (Bruker BioSpin GmbH, Germany) equipped with a ^{1}H transmit-receive volume coil with active detuning with an inner diameter of 82 mm and a bore length of 112 mm was used to evaluate temperature (37 and 70 °C), static or dynamic culturing, and degradation process (hydrolysis or enzymatic) as main variables affecting PLGA degradation. A first set of samples (SPION-PLGA fibers) was incubated at different temperatures (37 and 70 °C) and subjected to either static or dynamic culturing conditions for 4 weeks. A second set of samples was incubated at fixed 37 °C, but exposed to i) a slightly acidic environment, ii) enzymes, iii) a combination of both. All samples were imaged every one week. All MRI images presented in this study were acquired axially. Qualitative ^{1}H-T$_2$-weighted images were acquired using a fast spin echo sequence [Repetition time (TR): 2197 ms; Echo time (TE): 80 ms; echo spacing: 26 ms; acceleration factor: 8; matrix size; 180 x 180; Field of view (FOV): (25 x 25) mm^2; slice thickness; 5 mm; total acquisition time: 6 min]. The degradation of the SPION-PLGA coating was quantified by the decrease in transverse relaxation times (T$_2$), measured using a 2D multi-slice, multi-echo spin-echo (MSME) sequence with a 90° excitation pulse followed by a train of equally spaced 180° refocusing pulses [TR: 3742 ms; TE: 20 ms; echo spacing: 20 ms; echo images: 30; number of averages: 4; matrix size: 100 x 100; FOV: (25 x 25) mm^2; slice thickness: 5 mm; total acquisition time: 25 min]. T$_2$ relaxation times and the corresponding R2 relaxation rates (T$_2^{-1}$) were calculated using Imalytics Preclinical Software (Gremse-IT GmbH, Aachen, Germany) by fitting an exponential curve to the signal amplitudes as a function of the TE for each segmented region of interest (ROI). Equation (1) was used for the fitting of the exponential curve:

$$M = M_0 \; e^{-\frac{TE}{T2}} + C \tag{1}$$

The offset (C) was included to account for a signal plateau created by noise or a component with slow signal decay. The relaxation rate R$_2$ was calculated as the inverse of T$_2$.

Additionally, R$_2$ colormaps were obtained after voxel-wise fitting of equation (1) using the ParaVision 7 preclinical imaging software (Bruker BioSpin GmbH, Germany).

2.4. In vitro characterization of the textile scaffold and TEVGs by hybrid ^{1}H/^{19}F MRI

2.4.1. ^{19}F-TPU characterization

The Bruker 7 T MRI scanner equipped with a ^{1}H/^{19}F transmit-receive volume coil (72 mm of inner diameter and 112 mm of bore length) with active detuning was used. First, the ^{19}F-TPU granules (Lubrizol, Wickliffe, Ohio, United States) were tested alongside a water phantom. Subsequently, non-localized spectra of ^{19}F were acquired with an NSPECT sequence [TR: 1000 ms; flip angle: 30°; number of acquisition points: 10000; bandwidth: 353.87 ppm; averages: 30; total acquisition time: 30 s]. The spectra showed one defined peak at −84 ppm and one smaller side peak at −78 ppm, indicating that not all fluorine atoms in the ^{19}F-TPU polymeric chain are equivalent. For all following ^{19}F-TPU image acquisitions, the offset frequency was set to −24.000 Hz from the ^{1}H peak. Prior to performing the ultrashort echo time (UTE) imaging, the gradient trajectories were measured using the ^{1}H signal. ^{19}F-UTE imaging [TR: 30.000 ms; Echo time (TE): 0.296 ms; flip angle: 15.0°; averages: 30; matrix size: 32 × 32; FOV: (25 × 25) mm^2; slice thickness:

5 mm; total acquisition time: 9 min] was applied. Mean calculated ^{19}F-TPU signal intensities within ROIs were measured and normalized to the standard deviation (σ) of the noise (measured in the background).

Later, to assess the concomitant visibility of both ^{1}H and ^{19}F signals, MRI phantoms were produced by placing the obtained ^{19}F-TPU threads and fibers in a 15 mL falcon tube filled with water. ^{19}F signals were acquired using the ^{19}F-UTE sequence mentioned above with 90 averages. Qualitative ^{1}H-T$_2$-weighted images were acquired using a fast spin echo sequence [TR: 2197 ms; TE: 80 ms; echo spacing: 26 ms; acceleration factor: 8; matrix size; 180 x 180; FOV: (25 x 25) mm^2; slice thickness; 5 mm; total acquisition time: 6 min]. Imalytics Preclinical Software (Gremse-IT GmbH, Aachen, Germany) was employed for all the image analyses.

2.4.2. Enhancing ^{19}F-TPU fiber visibility

To find an optimum ^{19}F-UTE image quality, i.e., good signal-to-noise ratio (SNR), while keeping overall scan time within reasonable limits, a systematic investigation was performed to determine the amount of ^{19}F-TPU that needs to be incorporated in our vascular prosthesis textile scaffolds. Therefore, 1, 2, and 4 ^{19}F-TPU fibers were sewn on top of the prosthetic textile scaffold, which was initially composed of PVDF warp-knitted fibers and 0.2 % (w/w) SPION-PLGA coating. The samples were placed in a 15 mL falcon tube filled with water and monitored by employing the previously used ^{1}H-T$_2$-weighted and ^{19}F-UTE sequences.

2.4.3. Longitudinal monitoring of vascular prosthesis remodeling

As shown in Fig. 3, ^{19}F-TPU fibers were knitted onto the SPION-PLGA and PVDF textile scaffolds following three different designs (Design 1: four single ^{19}F-TPU fibers positioned at quarter points; Design 2: two couples of ^{19}F-TPU fibers positioned at half points; and Design 3: four couples of ^{19}F-TPU fibers positioned at quarter points). With these three designs, we aimed to investigate whether the ^{19}F SNR was influenced not only by the number of fibers within the FOV but also by their proximity or distance from each other. The samples were incubated in sterile PBS at 37 °C for 3 weeks. The same ^{19}F-UTE and ^{1}H-T$_2$-weighted sequence parameters were employed as during the above-described phantom measurements. T$_2$ relaxation times and the corresponding R$_2$ relaxation rates (T$_2^{-1}$) were calculated as previously described for the SPION-PLGA fiber degradation study.

2.4.4. Assessing the biocompatibility of the ^{19}F-TPU fibers

To investigate whether the novel ^{19}F-TPU fibers were biocompatible with the cellular components present in our vascular prosthesis, an in vitro cytotoxicity XTT assay was performed. HUASMCs and HUAECs were separately cultivated in sterile 24 well plates (Thermofisher Scientific, Massachusetts, USA) upon confluency. Subsequently, the cells were exposed to sterile SPION-PLGA and ^{19}F-TPU fibers using cell culture inserts with a pore size of 8.0 μm (Corning GmbH, Kaiserslautern, Germany) for 24 h. A negative control consisted of HUASMCs and HUAECs exposed to empty inserts. The colorimetric assay was quantitatively measured using a Tecan Infinite® 200 microplate reader (Tecan, Männedorf, Switzerland).

2.4.5. Longitudinal monitoring of TEVGs

TEVGs were monitored by hybrid ^{1}H/^{19}F MRI immediately after endothelialization of their lumen (day 1) as well as after 3 and 7 days. Prior to the MRI measurements, the bioreactor tubings containing the TEVGs were disconnected and clamped to facilitate placing the samples within the MRI bore. The same MR sequences as mentioned before, i.e., ^{1}H-T$_2$-weighted, ^{1}H-T$_1$-weighted, and ^{19}F-UTE sequences for imaging and ^{1}H MSME for T$_2$-mapping, were employed.

2.5. In vivo longitudinal hybrid assessment of implanted TEVGs

2.5.1. Subcutaneous implantation

Three inbred male Lewis rats (Janvier Labs, Le Genest-Saint-Isle,

France) of 12 weeks of age were employed for the evaluation and longitudinal monitoring of our vascular prostheses. Anesthesia was induced with 4–5 vol% of isoflurane combined with an O_2 flow rate of 4–5 L mL^{-1} and maintained with 2.5–3 vol% of isoflurane and 1 mL^{-1} of O_2. After shaving the dorsum of the animals and applying an antiseptic spray, 2 mg kg^{-1} of Ropivacaine was injected to ensure local anesthesia. SPION-PLGA coated PVDF scaffolds additionally labeled with ^{19}F-TPU and containing syngeneic rat SMCs and ECs (TEVG_SPION-TPU) and their counterpart lacking SPIONs labeling (TEVG_TPU) were inserted in 1.5 cm pouches obtained below the skin on the right and on the left part of the rat dorsum, respectively. The ^{1}H/^{19}F MRI longitudinal investigation was performed under isoflurane anesthesia on days 1, 7, 14, and 21 after the subcutaneous implantation of the TEVGs. The animals were euthanized after 21 days to perform histological analyses.

^{1}H-T_2-weighted and ^{1}H-T_1-weighted anatomical images were acquired using a T_2-weighted fast spin echo sequence [TR: 1300 ms; TE: 25 ms; echo spacing: 8.3 ms; acceleration factor: 8; matrix size: 180 x 180; FOV: (70 x 70) mm^2; slice thickness: 5 mm; total acquisition time: 4 min] and a T_1-weighted fast spin echo sequence [TR: 200 ms; TE: 2.9 ms; flip angle: 30°; matrix size: 180 x 180; FOV: (70 x 70) mm^2; slice thickness: 5 mm; total acquisition time: 5 min], respectively. T_2 relaxometry was performed using a MSME sequence [TR: 4123 ms; TE: 6.4 ms; echo spacing: 6.4 ms; echo images: 40; number of averages: 1; matrix size: 144 x 80; FOV: (70 x 70) mm^2; slice thickness: 5 mm; total acquisition time: 5 min]. To decrease the total scan time, the number of averages for the ^{19}F-UTE sequence was decreased from 90 to 50 while maintaining sufficient SNR.

2.5.2. Aortic TEVGs implantation

As a proof of concept, 2 Lewis male rats of ~350 g weight underwent laparotomy to insert TEVGs as aortic vascular grafts in the infrarenal region of the abdominal aorta. One animal received the TEVG_SPION-TPU, the other one TEVG labeled with only SPION-PLGA (TEVG_-SPION). Briefly, the animals received pre-surgery analgesia by 5 mg kg^{-1} s.c. Injection of carprofen®. The analgesic effect was assured for at least 3 days after the surgery. After induction of the anesthesia by isoflurane inhalation, the animals were intubated using a Viggo endotracheal tube (Viggo Medical Devices, New-Dehli, India) to ensure mechanical ventilation throughout the entire surgical procedure. After shaving and disinfecting the area of interest, the abdominal cavity was opened, and the abdominal aorta was exposed and separated. The TEVGs were sutured onto the native arterial wall. Subsequently, the patency of the vascular prosthesis was tested by ligating the abdominal aorta at the TEVGs insertion area and removing the upstream surgical clamp. The amount of lost fluid throughout the surgery was replaced by saline. The wound was sutured and disinfected, and the animals were monitored closely for the following days. ^{1}H/^{19}F MRI and ultrasound (US) were performed under isoflurane anesthesia on days 4, 11, and 18 after the surgery (day 0). The animals were euthanized after 18 days to perform histological analyses.

Respiratory gating was applied to the same MR sequences used during the previous in vivo study (subcutaneous TEVGs) to reduce motion artifacts while monitoring TEVGs implanted in the infrarenal region of the abdominal aorta. US imaging was performed using a VEVO 3100 preclinical US system equipped with a linear-array-MX-250 transducer (FUJIFILM VisualSonics, Toronto, Ontario, Canada). The US investigation was performed by placing the transducer perpendicularly to the floor and on the right side of the animal, allowing sagittal view of the TEVG and ligated rat abdominal aorta. The patency of the TEVGs as aortic vascular grafts in the infrarenal region of the abdominal aorta was assessed in B-mode at 21 MHz frequency, 4 % power, and 100 frames. Power Doppler US was used to detect blood flow within the implanted TEVGs at 16 MHz frequency, pulse repetition frequency 25 kHz, Doppler gain 36 dB, 100 % power, and 100 frames. The echo power was calculated as a percentage related to 100 % vascularity by drawing an ROI on TEVGs and ligated abdominal aortas using the VevoLAB software version 5.2 (FUJIFILM

VisualSonics, Toronto, Ontario, Canada).

2.6. Mass spectrometry investigation of SPION-PLGA fiber degradation

Paraffin-embedded samples collected during in vitro and in vivo evaluation of our TEVGs were coated with α-cyano-4-hydroxycinnamic acid (Bruker Daltonic, Germany) as a matrix (10 mg mL^{-1} dissolved in 70 % ACN/0.2 % TFA). The coating process was performed using a MALDI imaging sprayer (HTX TM-Sprayer: TMSP-M3, HTX Technologies, USA). MALDI data were accumulated using a TOF-TOF-mass spectrometer (Rapiflex; Bruker-Daltonic, Bremen, Germany) equipped with a SmartbeamTM 3D laser with a 10 kHz repetition rate and controlled by the Flex-Control 4.0 (Bruker-Daltonic, Germany). Mass spectra were acquired with 1200 laser shots for each raster point and a digitizer rate of 5.0 GS s^{-1} in reflector-positive and a mass range of 300-3200 Da.

Data analysis was performed using SCiLS Lab software (SCiLS Lab-2022b; SCiLS GmbH; Bremen, Germany) and Flex-Analysis 4.0 (Bruker-Daltonic, Bremen, Germany). MALDI MSI raw data sets were converted to the SCiLS SL file format. The baseline was calculated by an iterative top hat, and normalization was performed based on the total ion count (TIC) method. Peptides were identified through the MS/MS spectra using the lift option of the Rapiflex mass spectrometer (Bruker-Daltonic, Bremen, Germany). The mass spectra were calibrated and annotated using BioTools 3.2 (Bruker-Daltonic, Bremen, Germany) in combination with SwissProt (University of Geneva, Switzerland) and the MASCOT 2.2 database (Matrix Science, London, UK) comparing experimental mass-spectrometric data with calculated peptide masses for each entry into the sequence database.

2.7. Histology

All the samples were fixed in Carnoy's solution and embedded in paraffin blocks. A microtome (Microm HM 430, Thermofisher Scientific, Massachusetts, USA) was used to obtain 5 μm thick sections, which were later collected from a water bath using glass object slides (Thermofisher Scientific, Massachusetts, USA). Prior to adding the primary antibodies of choice, the samples were deparaffinized with xylene and ethanol, blocked and permeabilized using 5 % normal goat serum (Agilent Dako, Santa Clara, California, USA) mixed with 0.1 % Triton X-100 aqueous solution. The primary antibodies were incubated at room temperature for 1 h (anti-rat and human α-smooth muscle actin (αSMA), anti-rat and human elastin, anti-rat collagen I, anti-rat and human collagen III, anti-rat and human collagen IV, anti-rat F4/80, and anti-rat CD3; Acris Antibodies GmbH, Herford, Germany; Abcam, Berlin, Germany; Thermofisher Scientific, Massachusetts, USA). After extensive washing with PBS, secondary antibodies were added at room temperature for 45 min (Alexa Fluor 488 and Alexa Fluor 594 labeled anti-mouse IgG and anti-rabbit IgG antibodies; Thermofisher Scientific, Massachusetts, USA). DAPI (Thermofisher Scientific, Massachusetts, USA) was used to stain the nuclei. The slides were mounted using a fluorescent mounting medium (Agilent Dako, Santa Clara, California, USA). A different protocol was used to stain F4/80 and CD3. After blocking and permeabilization, samples were incubated with anti-F4/80 or anti-CD3 (Bio-Rad, Düsseldorf, Germany, and Abcam, Berlin, Germany) at room temperature for 1 h. After washing, anti-Horseradish Peroxidase (HRP) secondary antibodies (Abcam, Berlin, Germany) were applied at room temperature for 45 min. As following step, a Cy5 tyramine signal amplification (TSA)-conjugated dye (PerkinElmer, USA), diluted with an amplification diluent buffer (PerkinElmer, USA), was added for 10 min. DAPI (Thermofisher Scientific, Massachusetts, USA) was added for 5 min to stain the nuclei. After washing, the slides were mounted with Mowiol (Carl-Roth, Karlsruhe, Germany) mixed with DAPI (Merck, Germany).

To perform H&E staining, samples were incubated with Eosin G 0.5 % in water for 30 min, followed by extensive washing under running water for 20 min to stain the ECM components. Hematoxylin was added for 5 min to stain the nuclei (Eosin G 5 % and Hematoxylin, Carl Roth

GmbH, Karlsruhe, Germany).

Masson's trichrome and Von Kossa staining were performed using a Masson's trichrome stain kit (Abcam, Berlin, Germany) and Von Kossa stain kit (Abcam, Berlin, Germany), respectively, following the instructions of the manufacturer.

2.8. Microscopy

An Axio Imager M2 fluorescence microscope equipped with an AxioCam MRm Rev.3 camera (Carl-Zeiss, Oberkochen) with a magnification of $20\times$ and Vectra® 3.0 Microscope Automated Quantitative Pathology Imaging were used to acquire representative images of stained tissue sections. Images were quantified via Fiji software (ImageJ, NIH) and inForm (Akoya Biosciences, Marlborough, Massachusetts, USA).

2.9. Statistical analysis

All in vitro samples were prepared and analyzed in triplicate (sample size = 3). For the in vivo subcutaneous study, power analysis was additionally performed using G* Power software (version 3.1.9.2) with a significance level of 0.05 (α err prob – type I error) and a statistical power of 0.8 (power 1-β err prob – type II error). This analysis indicated that 3 animals per group were necessary to ensure a significant difference of 20 % with a standard deviation of 5 %. In adherence to the principles of the 3Rs, i) 3 animals were used (Reduce), ii) to allow each animal to serve as its own sample and control simultaneously, TEVGs

labeled with both ^{19}F-TPU and SPIONs were implanted on the right side of the animal dorsum, and control TEVGs labeled with only ^{19}F-TPU were implanted on the left side (Reuse), and iii) syngeneic cells were harvested from these animals at the end of the longitudinal experiment to produce new TEVGs for future animal experiments (Recycle).

The results are presented as mean values ± standard deviations (SD). The analysis was performed using GraphPad Prism 8 (GraphPad Prism Software, San Diego, California, USA). The statistical comparison of two groups was performed using Student's t-test, while for multiple group analyses, one-way ANOVA (one-tailed) with a post-hoc correction test (Tukey) was applied as recommended by the software. Statistical significance was considered for values $p \leq 0.05$.

For the in vivo implantation of TEVGs in the infrarenal region of the abdominal aorta, no group comparison and statistical significance were performed due to the use of only 1 animal per group.

3. Results

3.1. Characterization of ^{19}F-TPU by hybrid ^{1}H/^{19}F MRI

The highly fluorinated polymer ^{19}F-TPU was intended to be used as permanent scaffold material. To better understand its MRI properties, it was first characterized in the form of rough granules, then as threads of approximately 3 mm, and finally as thin fibers of circa 1.5 mm diameter, as illustrated in Fig. 2A–C. The different production stages, from granules to polymeric fibers, significantly influenced MRI visibility, as
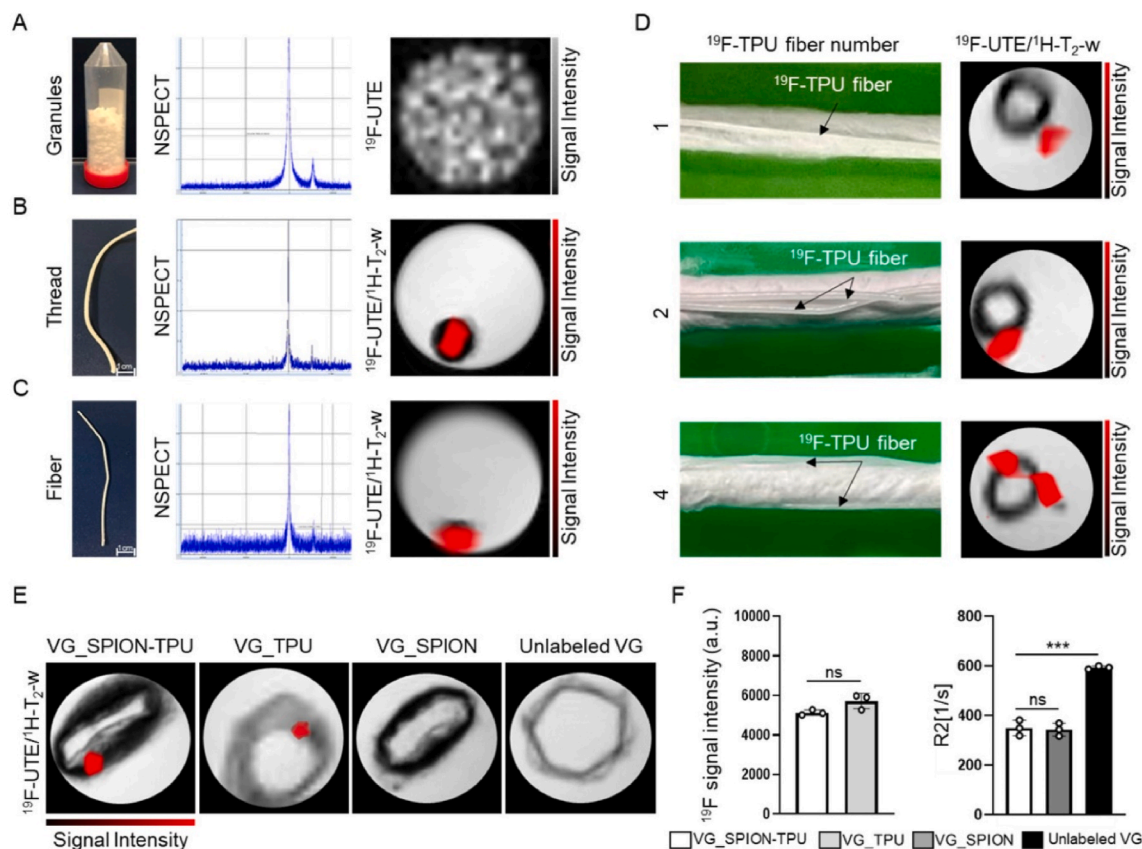

Fig. 2. Scaffold characterization with MRI. A-C) MR phantoms containing ^{19}F-TPU in the form of granules (A), threads (B), and fibers (C) exhibit the same NSPECT spectra, but with background noise that is inversely proportional to the amount of ^{19}F-TPU present in the sample. The ^{19}F-UTE "hot iron" images overlaying on grayscale ^{1}H-T$_2$-weighted images reflects the ^{19}F content within the phantoms. However, even for a single fiber, a distinct peak above the background noise is still detected. D) PVDF scaffolds coated with SPION-PLGA were additionally labeled with 1, 2, and 4 ^{19}F-TPU fibers, respectively. Hybrid ^{1}H/^{19}F MRI allows the detection of single ^{19}F-TPU fibers also in combination with other textile components. The ^{19}F signal improves if two or more fibers are positioned adjacently, due to the increase in ^{19}F-TPU per voxel. E) ^{19}F-UTE superimposed on ^{1}H-T$_2$-weighted images of VG_SPION-TPU, VG_SPION, and unlabeled VG show no interference or quenching between the two MR labels. F) Quantitative R$_2$ analyses confirm that SPION-PLGA does not influence the ^{19}F-TPU signal. All values were obtained in triplicates and are presented as means ± SD; One-way ANOVA with Tukey post hoc correction was applied to compare groups, indicating p > 0.05 as ns, p < 0.05 as *, p < 0.01 as **, p < 0.001 as ***, and p < 0.0001 as ****. Scale bar: 1 cm.

evidenced by the NSPECT spectra and the signal intensity obtained by ^{19}F-UTE sequences (granules: 17389 a.u.; thread: 6401 a.u.; fiber: 5144 a.u.). However, a well-defined peak was still detected for single ^{19}F-TPU fibers by ^{1}H/^{19}F MRI, and a clear "hot spot" ^{19}F signal superimposed to a ^{1}H-T$_2$-weighted image was obtained by image post-processing with Imalytics Preclinical software.

Next, the ^{19}F-TPU fibers were evaluated as permanent imaging labels of mixed scaffolds consisting of a degradable (PLGA fibers) and a non-degradable component (PVDF scaffold). In this context, different ^{19}F-TPU fiber numbers and positions were considered to optimize scaffolds' visibility in MRI (Fig. 2D). For this purpose, ^{19}F-TPU fibers were knitted onto the pre-existing warp-knitted PVDF textile scaffolds, which were additionally coated with electrospun PLGA fibers. To increase the MRI visibility of the latter, otherwise lacking in contrast, 0.2 % (w/w) SPIONs were passively incorporated into the PLGA fibers' core during the electrospinning process as described previously [12]. Hybrid ^{1}H/^{19}F MRI confirmed the visibility of single ^{19}F-TPU fibers when combined with the other textile components, which may influence the detection of ^{19}F signal via susceptibility artifacts, i.e., blooming artifacts, that cause distortions or local signal changes. Furthermore, it was beneficial to cluster two or more ^{19}F-TPU fibers to increase the ^{19}F content per voxel (1 fiber: 5355 ± 49.7 a.u.; 2 fibers: 5821 ± 40.9 a.u.; 4 fibers: 7684 ± 29.6 a.u.), rather than having them evenly distributed over the scaffold.

To exclude an influence of SPION-PLGA on the ^{19}F-TPU contrast, we measured the ^{19}F-TPU signal intensity and T$_2$ relaxation rates (R$_2$) of vascular grafts consisting only of textile scaffold without cellular components (VG). We produced different phantoms as follows: 1) VG containing both MR labels, SPIONs and ^{19}F-TPU fibers (VG_SPION-TPU), 2) VG lacking the ^{19}F-TPU (VG_SPION), 3) VG without SPIONs (VG_TPU),

and 4) unlabeled VG consisting of only MRI non-visible polymers. As shown in Fig. 2E and F, the presence of the grafts' components, especially SPIONs, did not influence the ^{19}F-TPU signal intensity (VG_SPION-TPU: 5128 ± 44 a.u vs. VG_TPU: 5711 ± 317.2 a.u.) and the presence of ^{19}F-TPU did not alter the R$_2$ values of the samples (VG_SPION-TPU: 349.8 ± 25.3 s^{-1}; VG_SPION: 317.7 ± 21.1 s^{-1}; unlabeled VG: 593.7 ± 5.6 s^{-1}).

3.2. Longitudinal investigation of the vascular prosthesis by hybrid ^{1}H/^{19}F MRI

After it was ensured that both MR labels were concomitantly detectable without impairment, we performed additional in vitro experiments to evaluate temperature (37 and 70 °C), static or dynamic culturing, and degradation process (hydrolysis or enzymatic) as main variables affecting PLGA degradation. Faster PLGA fiber degradation occurred at higher temperatures. Dynamic culturing also accelerated PLGA fiber degradation, particularly evident at 37 °C. Although no statistically significant differences were observed among samples exposed to pH 5, trypsin, or the combination of both, a faster PLGA fiber hydrolysis was noted compared to statically conditioned samples (Fig. S1, Supporting Information).

Subsequently, we investigated whether the resorption of SPION-PLGA fibers could be longitudinally monitored and the ^{19}F signal of the permanent scaffold component (^{19}F-TPU) remained stable. As previously described, ^{19}F-TPU fibers were knitted onto the SPION-PLGA and PVDF textile scaffolds following three different designs to further investigate the effects of SPION-PLGA degradation on ^{19}F signal detection (Fig. 3). ^{19}F-TPU fiber signal intensities measured by ^{19}F-UTE
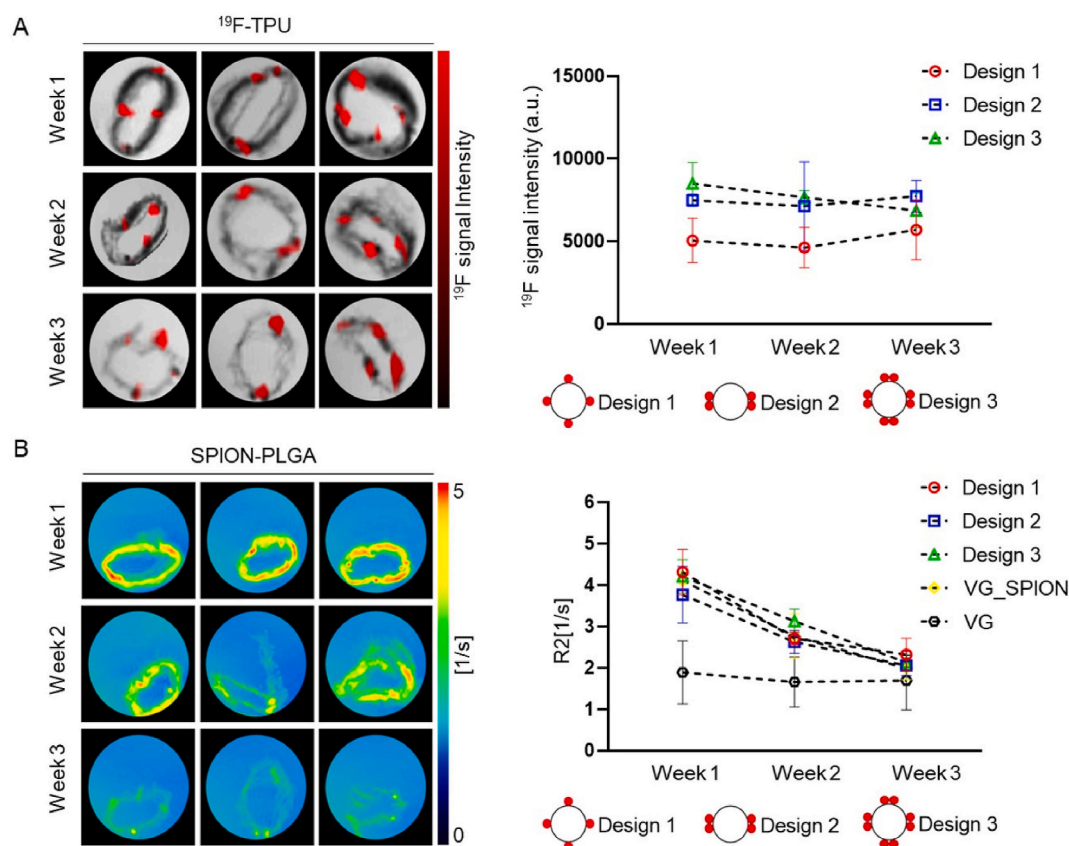

Fig. 3. Longitudinal evaluation of statically conditioned vascular prostheses. A) MR phantoms labeled with different numbers of ^{19}F-TPU fibers positioned in three different ways (Design 1–3). ^{19}F-UTE superimposed on T$_2$-weighted images show no statistically significant changes in ^{19}F-TPU fibers' signal intensity after 3 weeks of monitoring. B) R$_2$ colormaps superimposed to ^{1}H-T$_2$-weighted images show gradual degradation of the SPION-PLGA fibers in combination with ^{19}F-TPU fibers (VG_SPION-TPU Design 1–3) and without (VG_SPION). R$_2$ relaxometry confirms the SPION-PLGA degradation in comparison to the unlabeled counterpart. All values were obtained in triplicates and are presented as means ± SD; One-way ANOVA with Tukey post hoc correction was applied to compare groups.

sequence did not significantly change, indicating that the ¹⁹F-TPU remained stable over the observation period (Fig. 3A; Table S1, Supporting Information). In contrast, PLGA fibers degraded throughout the observation time, which is clearly visible in R_2 colormaps superimposed to ¹H-T₂-weighted images (Fig. 3B; Table S1, Supporting Information). VG_SPION and unlabeled VG were used as additional negative controls (Fig. 3B; Table S1, Supporting Information). As postulated, the MR signal of ¹⁹F-TPU remained constant throughout the observation period and was not influenced by the degrading SPION-PLGA fibers.

XTT cytotoxicity assays were employed to assess the biocompatibility of the ¹⁹F-TPU fibers. As previously described, HUASMCs and HUAECs were exposed to the ¹⁹F-TPU and SPION-PLGA fibers. Cells exposed to empty cell inserts were used as a negative control. The XTT revealed no difference in cell viability between both ¹⁹F-TPU fiber exposed HUASMCs (100.3 ± 4.6 %) and HUAECs (97.3 ± 6.6 %) and unexposed negative control cells (HUASMCs: 101.4 ± 0.9 %; HUAECs: 95.4 ± 5.2 %) (Fig. 4A). SPION-PLGA fibers were also biocompatible but insignificantly tended to lower cell viability, as it was expected due to the generation of acidic degradation products (SPION-PLGA HUASMCs: 92.3 ± 3.2 %; SPION-PLGA HUAECs: 93.5 ± 9.7 %).

After confirming the biocompatibility of the imaging labels incorporated into the textile scaffold of our vascular prostheses and the

decision that Design 2 is ideal with respect to manufacturing and MR signal, complete biohybrid tissue-engineered vascular grafts (TEVGs) were produced by molding the textile scaffold with fibrin gel containing HUASMCs and introducing HUAECs for the endothelialization of the lumen. To longitudinally investigate the ¹⁹F-TPU permanent MR signal and SPION-PLGA resorption, TEVGs were dynamically conditioned for 0, 3, and 7 days. No statistically significant changes in terms of ¹⁹F-TPU fiber signal intensity were observed via ¹⁹F-UTE and ¹H-T₂-weighted images superimposition (day 0: 7818 ± 1158 a.u.; day 3: 7106 ± 712.4 a.u.; day 7: 8701 ± 1196 a.u.) (Fig. 4B and C). Due to the presence of cellular components, a faster PLGA fibers degradation and, thus SPIONs release, was detected via a gradual decrease in the R_2 values depicted via quantitative R_2 colormaps (day 0: 4.8 ± 0.3 s^{-1}; day 3: 3.8 ± 0.3 s^{-1}; day 7: 2.7 ± 0.1 s^{-1}). The presence of cells and their metabolic and enzymatic activity contribute to the decrease in microenvironmental pH, which enhances the acidic hydrolysis of the PLGA fibers in comparison to previous samples containing no cells. Further histological analyses were performed to assess the impact of the presence of ¹⁹F-TPU fibers on ECM components' production and deposition within our TEVGs with a particular focus on collagen I, III, and IV, and αSMA (Fig. S1, Supporting Information). For all these matrix components, a gradual increase in production and deposition was observed on day 7 in
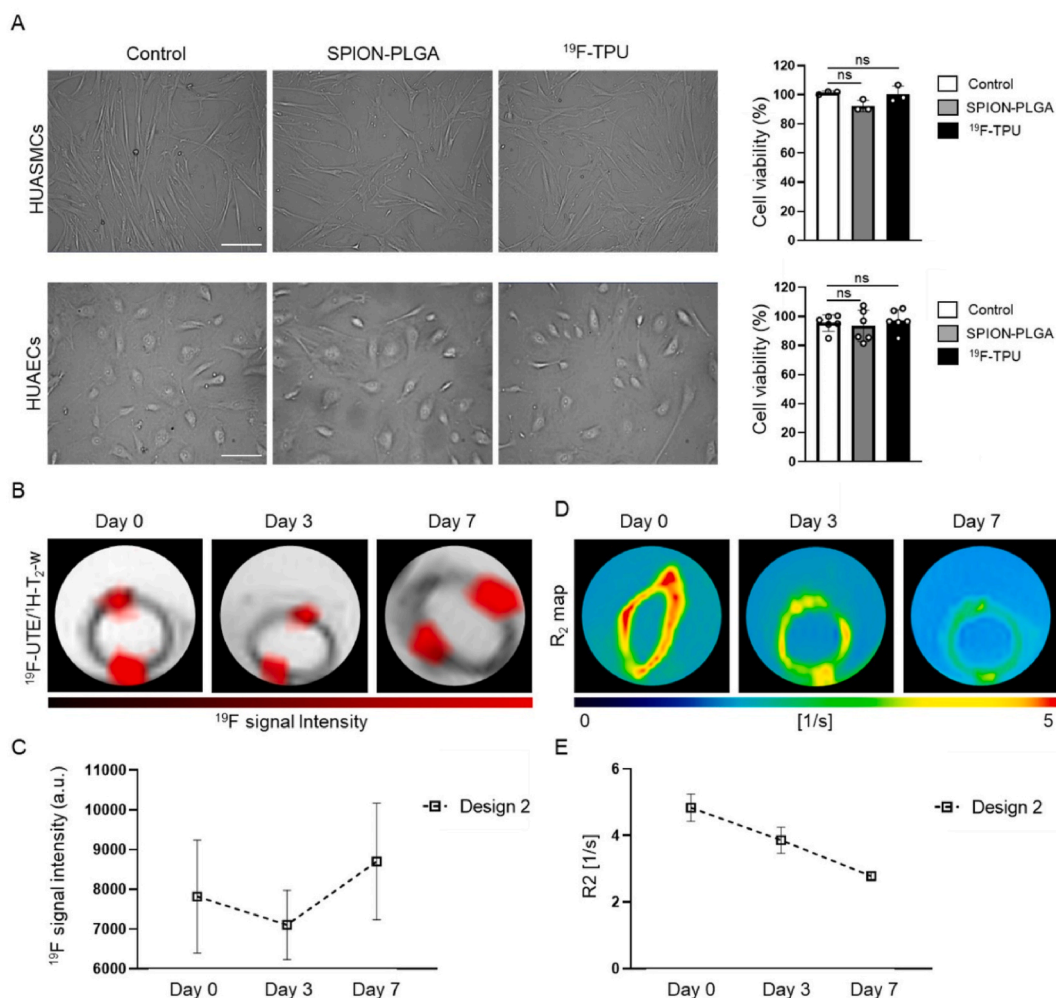

Fig. 4. Evaluation of ¹⁹F-TPU biocompatibility and longitudinal monitoring of TEVGs under dynamic conditioning. A) Representative images of HUASMCs and HUAECs exposed to empty cell inserts, SPION-PLGA, or ¹⁹F-TPU fibers. XTT shows no statistically significant differences in cell viability in both types of cells among the three groups. B) ¹⁹F-UTE superimposed on grayscale ¹H-T₂-weighted images of TEVGs cultured for 7 days. C) ¹⁹F-TPU related MR signal intensities remained stable over time. D-E) R_2 colormaps display gradual degradation of SPION-PLGA fibers. All values were obtained in triplicates and are presented as means ± SD; One-way ANOVA with Tukey post hoc correction was applied to compare groups, indicating $p > 0.05$ as ns, $p < 0.05$ as *, $p < 0.01$ as **, $p < 0.001$ as ***, and $p < 0.0001$ as ****. Scale bar: 500 μm.

comparison to day 0 (no bioreactor conditioning). Furthermore, a comparably increasing presence of major ECM components was observed in TEVGs containing both SPION-PLGA and ^{19}F-TPU (TEVG_-SPION-TPU) and TEVGs only labeled with SPION-PLGA (TEVG_SPION), again confirming the biocompatibility of the ^{19}F-TPU fibers. Elastin production and deposition were additionally investigated (Fig. S2, Supporting Information). In contrast to the human umbilical artery, used as a positive control, no elastin fibers were present in all TEVGs, which is in line with previous findings [12].

3.3. Longitudinal in vivo evaluation of TEVGs by hybrid $^1H/^{19}F$ MRI

To confirm the in vivo translatability of our imaging approach and to ensure the permanent visibility of the ^{19}F-TPU fibers in vivo, three Lewis male rats were subcutaneously engrafted with TEVGs containing both MR labels, namely TEVG_SPION_TPU and TEVGs lacking SPIONs labeling (TEVG_TPU). The latter were used as a negative control to investigate the influence of SPIONs on the visibility of the ^{19}F-TPU fibers. As illustrated in Fig. 5A, the TEVG_SPION_TPU samples (in red) were subcutaneously implanted on the right side of the dorsum of the animals, while the TEVG_TPU counterparts (in blue) were engrafted on the left side. ^{19}F-TPU fibers remained visible without significant changes in signal intensity by hybrid $^1H/^{19}F$ MRI with no differences between TEVG_SPION-TPU and TEVG_TPU indicating that the SPIONs did not affect the ^{19}F MR signal (Fig. 5B; Table S2, Supporting Information). TEVG_SPION_TPU showed higher R_2 values than the TEVG_TPU counterpart due to the substantial decrease in T_2 generated by SPIONs (Fig. 5C; Table S2, Supporting Information). In comparison to the TEVG_TPU, whose R_2 values remained constant, in TEVG_SPION_TPU, R_2 progressively decreased throughout the observation time (Fig. 5C; Table S2, Supporting Information). The body weight of the rats, expressed in grams (g), was not altered over the examination period indicating that their well-being was not strongly impaired and highlighting the biocompatibility of the implanted prostheses (Fig. 5D).

TEVG_SPION-TPU and their TEVG_TPU counterparts were harvested at the end of the in vivo longitudinal MR investigation (Fig. 6C and D). TEVGs only labeled with SPION-PLGA (TEVG_SPION) and their unlabeled equivalent lacking all MR labels were used as additional negative controls (Fig. 6A and B). The latter were unpublished samples from a previous study [12]. Ex vivo immunofluorescence and histological analyses were performed to further investigate TEVG_SPION_TPUs' impact on living organisms. Hematoxylin and eosin (H&E) stains show strong endogenous cellular infiltration and prosthesis colonization, facilitating its integration within the host organism (Fig. 6). The total amount of collagen was investigated via Masson's trichrome staining in parallel to collagen III and IV, as major ECM components known to strongly influence vascular prostheses functionality. An abundant presence of various collagen types was observed, highlighting the strong maturation process that TEVGs underwent in vivo. Since αSMA is important for the contractility of blood vessels and can influence the production and deposition of ECM components via paracrine signaling and mechanical interactions, syngeneic smooth muscle cells (SMCs), derived from mesenchymal adipose stem cells of donor animals, were incorporated into the fibrin gel of our TEVGs. αSMA was also strongly observed in all TEVGs. No statistically significant differences were observed among the samples for all analyzed markers, suggesting that our imaging labels do not disturb the remodeling process (Fig. S3, Supporting Information).

To investigate the immune reaction of the host organisms toward our four models of TEVGs, the total number of macrophages (F4/80 positive cells) and T-cells (CD3 positive cells) was evaluated. After 21 days of in vivo implantation, a comparatively low number of immune cells was observed across all samples. The low inflammation and few phagocytic macrophages present within our samples can be attributed to the reduced presence of PLGA debris, which was also confirmed via MS (see

Fig. S4, Supporting Information). Our TEVGs exhibited a lower immune response in comparison to synthetic grafts, known for their poor performance, compliance mismatch, and non-biocompatible composition [28–31]. Hence, synthetic grafts are characterized by graft failure rates between 70 % and 100 % at 10–15 years of long-term follow-up [32].

To further investigate the in vivo feasibility of our imaging approach and study the performance and integration of our TEVGs within the host organism, two Lewis male rats underwent laparotomy and were engrafted with TEVG_SPION_TPU and TEVG_SPION in the infrarenal region of the abdominal aorta, respectively. The surgery occurred on day 0, followed by MRI and US on days 4, 11, and 18 (Fig. 7A). The inner diameter of the TEVGs was further decreased to 1.5 mm to avoid a significant mismatch with the native vessel (Fig. 7B). As depicted in Fig. 7C, due to unexpected stiffness caused mainly by the four ^{19}F-TPU fibers, the design of the TEVGs textile scaffold had to be changed accordingly, integrating only one ^{19}F-TPU fiber. Furthermore, as evidenced by the photo taken on day 18, the TEVGs retained their shape even though completely integrated within newly deposited ECM and remained functional and patent until the end of the experiment. As expected, the MRI signal from the ^{19}F-TPU fiber was visible only for TEVG_SPION_TPU, while no ^{19}F signal could be detected for TEVG_-SPION. The ^{19}F MRI signal intensity of TEVG_SPION_TPU remained constant without any changes throughout the 18 days of observation time (Fig. 7D and E: TEVG_SPION_TPU day 1: 5185 a.u.; day 18: 5781 a. u.). On the other hand, SPION-PLGA of both TEVG_SPION_TPU and TEVG_SPION displayed decreasing R_2 values over time indicating degradable fibers resorption in both types of implanted TEVGs (Fig. 7D–F: TEVG_SPION_TPU day 1: 21.1 s^{-1}; day 11: 18.5 s^{-1}; day 18: 14.5 s^{-1}; TEVG_SPION day 1: 19.2 s^{-1}; day 11: 17.7 s^{-1}; day 18: 14.6 s^{-1}). Notably, it was increasingly challenging to visualize the TEVG_-SPION as the SPIONs signal gradually decreased, highlighting the significant advantage of labeling the grafts' scaffold with the permanent ^{19}F-TPU fibers. As shown in Fig. 7G, Power Doppler US was performed to additionally investigate perfusion of our TEVGs. Blood flow within the TEVGs was confirmed by calculating the echo power (%) in the vascular graft and comparing it with the ligated abdominal aorta (Fig. 7H: TEVG_SPION_TPU and TEVG_SPION: 28.1 %; ligated abdominal aortas: 1.9 %). As shown in Fig. 7I, the animals exhibited a reduction in body weights (g) by 10.3 % and 10.9 % for the rats implanted with TEVG_-SPION and TEVG_SPION_TPU, respectively. However, the weight loss can be attributed to the loss of fluids during surgery, a phenomenon observed in humans as well [33]. The well-being of both rats was reflected by the stabilization of the body weight within 7 days post-surgery. Further ex vivo histological analyses were performed to investigate TEVGs remodeling and integration within the host organism as well as new ECM deposition and possible loss of graft patency or graft calcification (Fig. 7J). H&E, alongside immunofluorescence staining for collagen III, αSMA, and elastin revealed abundant new ECM. Notably, elastin-positive cells were exclusively observed in TEVGs implanted in the infrarenal region of the abdominal aorta. Further elastin deposition and maturation into fiber-like structures may be detectable after longer monitoring. This aligns with our previous findings, where no elastin production was observed during 14 days of in vitro bioreactor conditioning and 21 days of subcutaneous implantation of TEVGs, respectively [12]. These data suggest that only the intense interplay between stronger mechanical stresses induced by arterial blood flow, constructive signaling molecules (i.e., matrix-bound nanovesicles), and inflammatory cells through the secretion of cytokines and growth factors stimulate a more intense remodeling of TEVGs, thus boosting an initial production of elastin. Von Kossa staining was additionally performed to investigate calcium deposits within the vascular prostheses and surrounding tissues. While Von Kossa staining detected calcification in the ligated rat abdominal aorta (RAA), no such deposits were observed within our vascular prostheses.
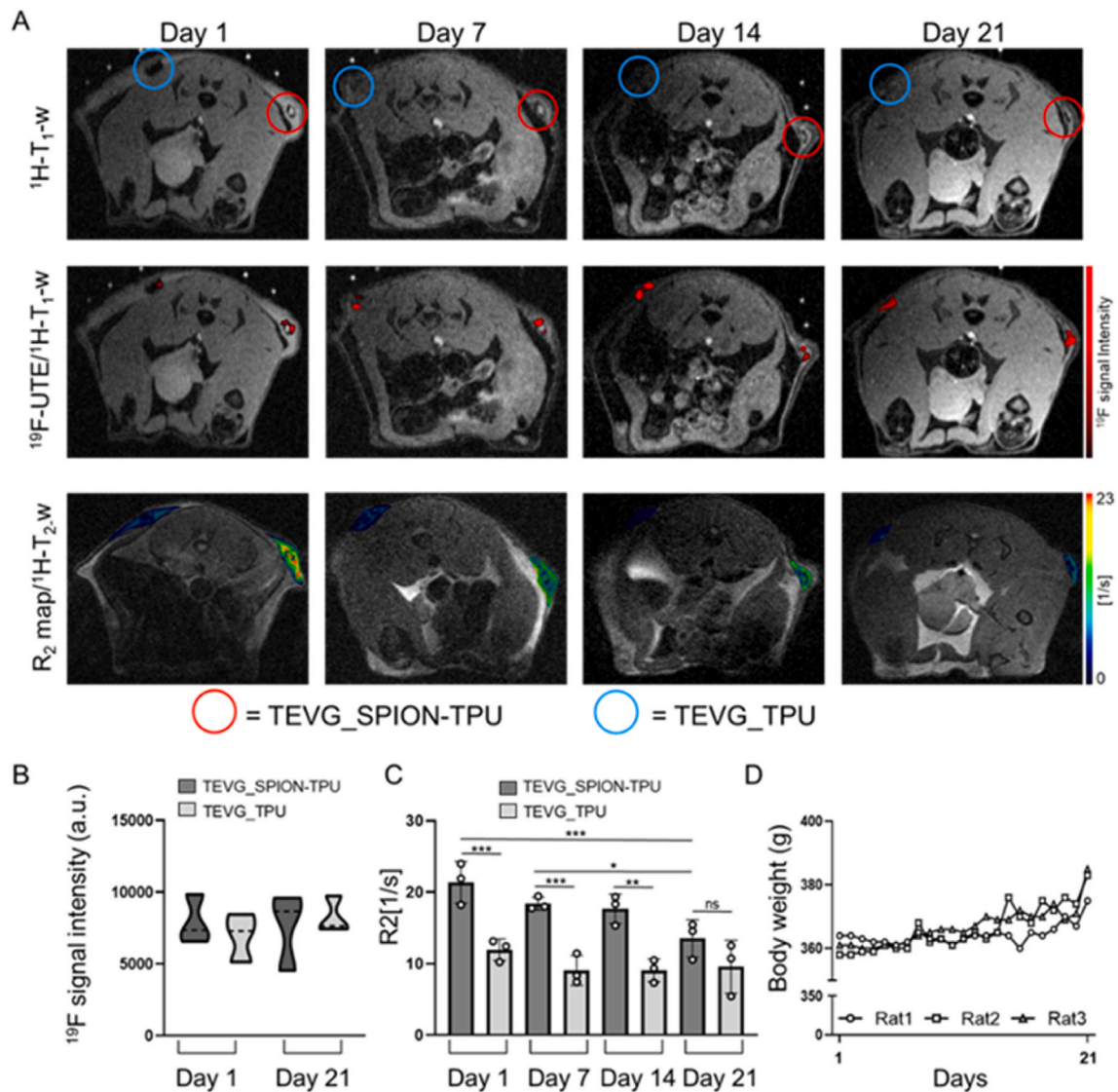
Fig. 5. Longitudinal in vivo monitoring of TEVGs by hybrid ^{1}H/^{19}F MRI. A) Representative ^{1}H-T$_1$-weighted images, ^{19}F-UTE superimposed on ^{1}H-T$_1$-weighted images, and R$_2$ colormaps superimposed on ^{1}H-T$_2$-weighted images show the temporal evolution of ^{19}F-TPU signal intensity and SPION-PLGA relaxometry throughout the 21 days of MR longitudinal monitoring. TEVG_SPION-TPU are encircled in red, whereas the samples highlighted in blue contain TEVG_TPU. B) The quantification of ^{19}F-TPU signal intensities of TEVG_SPION-TPU and TEVG_TPU samples at the beginning and end of the experiment reveal no significant alterations. The violin plot shows the frequency distribution of the data, and its width corresponds with the approximate frequency of data points in each region. C) R$_2$ relaxometry shows the degradation of the SPION-PLGA compared to plain PLGA throughout the 21 days of observation. D) Animal body weight was not negatively affected by the surgical procedure and the implanted prostheses. All values were obtained in triplicates and are presented as means $\pm$ SD; One-way ANOVA with Tukey post hoc correction was applied to compare groups, indicating $p > 0.05$ as ns, $p < 0.05$ as *, $p < 0.01$ as **, $p < 0.001$ as ***, and $p < 0.0001$ as ****. (For interpretation of the references to color in this figure legend, the reader is referred to the Web version of this article.)

It is crucial to note that this study provides only mere initial evidence of the potential applications of our imaging approach. Further studies are necessary to statistically validate these initial findings on larger animal cohorts.

4. Discussion

The field of tissue engineering is evolving toward more complex and multifaceted 3D constructs to meet the needs of the highly heterogeneous patient population. Here, TEVGs are promising as they enable high standardization on one hand, but also personalization, in vivo remodeling, and adaptation on the other. Furthermore, they can improve in vivo durability and reduce thrombogenic and adverse immunogenic effects, which often characterize fully synthetic grafts [34–37]. Biohybrid TEVGs are composed of a non-degradable synthetic

scaffold and a biodegradable and biocompatible textile component to allow prosthesis maturation. In our previous work, we developed a comprehensive imaging approach to enhance the MRI visibility and the possibility for long-term monitoring of the resorption of our biodegradable component, namely PLGA fibers, by passive incorporation of SPIONs [12]. We observed that the in vitro and in vivo resorption of the PLGA fibers correlated with the decrease of the R$_2$ values indicating the release of the SPIONs. Nonetheless, once the SPION-PLGA fibers were entirely degraded, we lost the information regarding the positioning and structural integrity of the implanted TEVGs. Therefore, we here suggest extending our imaging approach by knitting non-degradable ^{19}F-TPU fibers onto the pre-existing MRI inert PVDF scaffold.

Another aspect worth considering is that the production of autologous or syngeneic vascular grafts involves harvesting ECs and SMCs directly from patients. This approach offers immune compatibility, but
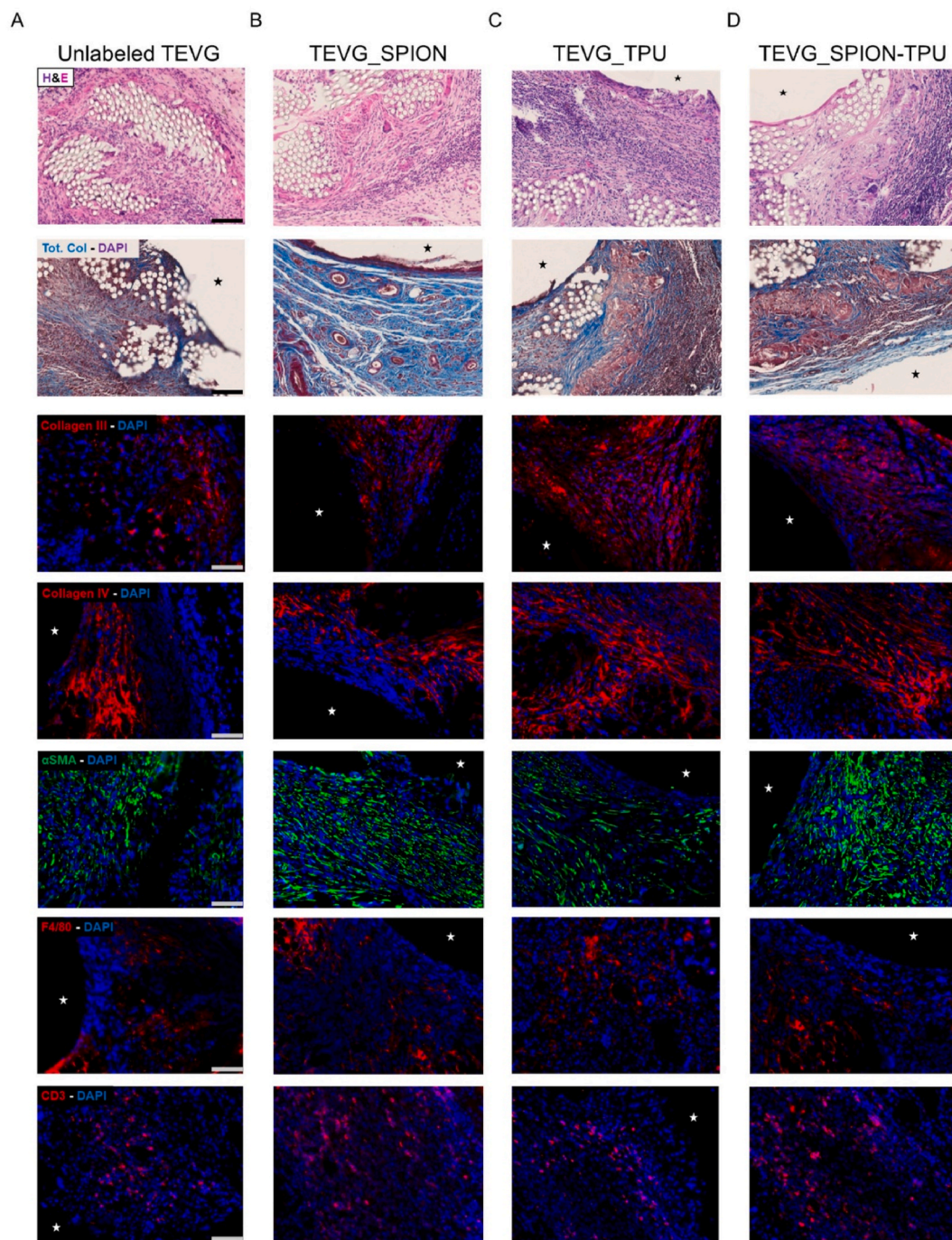
Fig. 6. Ex vivo histological analyses evaluating the effects of ^{19}F-TPU on ECM deposition and host reaction. A-B) Unlabeled TEVGs lacking both MR contrast agents used throughout this study (A) and TEVGs containing SPION-PLGA (TEVG_SPION, B) are used as negative controls. C) Vascular prostheses labeled with only the novel ^{19}F-TPU fibers (TEVG_TPU) were used as a supplementary negative control to exclude any additive, synergistic, or antagonistic effect between SPIONs and ^{19}F-TPU. D) Representative images of complete TEVGs labeled with both MR contrast agents, i.e., SPION-PLGA and ^{19}F-TPU fibers, (TEVG_SPION-TPU). H&E staining was performed to get an overview of ECM (in pink) and cell nuclei (in purple), highlighting the presence and infiltration of immune cells. The Masson's trichrome staining complementary shows total collagen in light blue, while nuclei are stained in purple. Fluorescence images in the bottom rows show collagen III and IV, F4/80, and CD3 in red, respectively, αSMA in green, and nuclei (DAPI) in blue. For all stainings no significant differences are observed, indicating that SPIONs incorporation into PLGA and ^{19}F-TPU does not change the body reactions after TEVGs implantation. Scale bar: 50 μm. The stars indicate TEVGs' lumen. (For interpretation of the references to color in this figure legend, the reader is referred to the Web version of this article.)

also implies invasive biopsies, limited cell quantity, and expensive and time-consuming culturing. Pluripotent/multipotent stem cells present a valuable alternative. For example, mesenchymal stem cells (MSCs) have been used to derive SMCs via chemical and mechanotransduction signals to mimic the tunica media of native vessels and secret anti-inflammatory factors [38]. However, harvesting enough MSCs remains challenging,

and moving toward progenitor cell in vivo maturation and differentiation requires a deeper understanding of their biointerfaces and crosstalks. These hurdles prompted interest in the production of in situ off-the-shelf implants. To confer immunocompatibility and off-the-shelf availability, grafts are processed via decellularization, depleting the cells but leaving the ECM architecture unmodified.
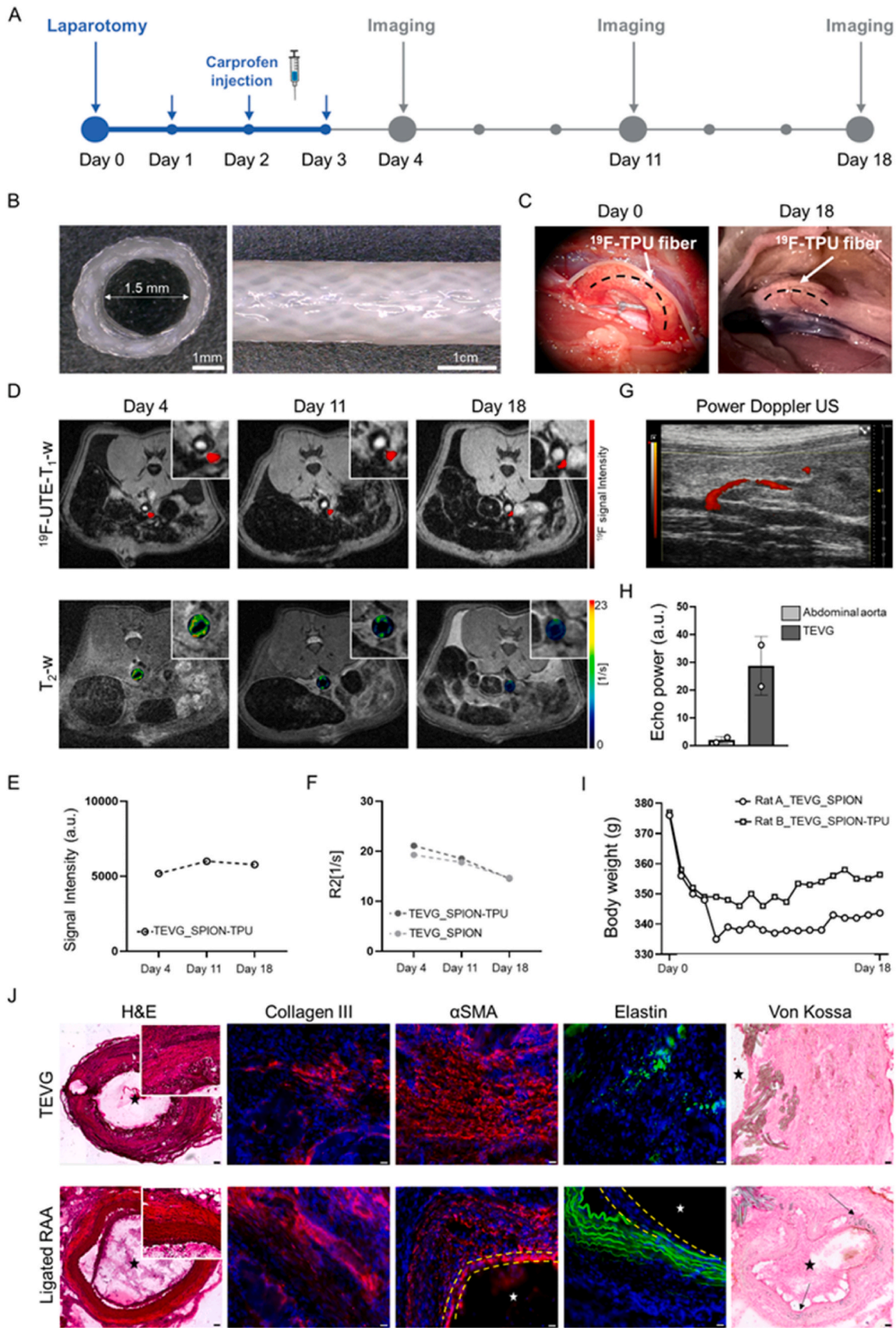
(caption on next page)

Fig. 7. Longitudinal in vivo monitoring of TEVGs implanted in the abdominal aorta. A) Schematic representation of the timeline of the animal experiments. B) Photos of a TEVG before implantation with inner diameter of 1.5 mm, wall thickness of 0.7 mm, and length of 4 cm, with the latter being decreased during the surgery at the discretion of the surgeons. C) TEVG implanted in the infrarenal region of the abdominal aorta labeled with only one ^{19}F-TPU fiber at day 0 and day 18. D) Representative ^{19}F-UTE superimposed on [1]H-T_1-weighted images show the permanent signal provided by the ^{19}F-TPU fiber. At the same time, R_2 colormaps superimposed on [1]H-T_2-weighted images demonstrate the SPION-PLGA degradation over time. E) The quantification of ^{19}F-TPU signal intensity of the TEVG_SPION-TPU confirms no significant change. F) R_2 relaxometry indicates the degradation of the SPION-PLGA in both TEVG_SPION_TPU and TEVG_SPION. G) Power Doppler US displays blood flow within the TEVGs. H) The echo power calculated from the Power Doppler videos indicates blood flow only within the TEVGs. I) A reduction of the animals' body weight was observed after surgery explained by the loss of liquids during the laparotomy. The animals started to stabilize and regain weight after the first week post-op. J) H&E (ECM in pink and nuclei in purple) as well as collagen III (in red), αSMA (in red), and elastin (in green) exhibit significant deposition of new ECM components and graft integration within the host organism. Dotted lines have been used to highlight the location of the intima where possible, aiming to clarify that αSMA and elastin are not expressed in the tunica intima of vessels but within the media. The presence of a small tunica intima may be attributed to underdevelopment within our TEVGs and damage in the ligated rat abdominal aorta (RAA). Von Kossa staining (calcification in black) depicts no calcium deposits that might impair the functionality of the vascular prostheses. In contrast, initial calcium deposits were observed in the ligated RAA, highlighted by the black arrows. H&E overview scale bar: 600 μm; Collagen III, αSMA, and elastin scale bar: 50 μm; Von Kossa scale bar: 200 μm. The stars indicate TEVGs' lumens. (For interpretation of the references to color in this figure legend, the reader is referred to the Web version of this article.)

Although the approaches of decellularization and recellularisation could potentially simplify the production of vascular prostheses, several studies suggested that decellularized scaffolds are more costly and could potentially elicit an immunogenic response, leading to graft failure, due to the presence of xenogeneic debris [39,40] Further research is needed to determine the most effective approach for achieving controlled tissue remodeling, scaffold degradation, selective cell recruitment, adhesion, and differentiation, leading to native-like tissues.

Despite our promising results, ^{19}F-TPU is characterized by elasticity and stickiness, hindering its spinnability. During our examinations, we observed that the stretching of the polymer during the production of thinner fibers is enough to cause a complete loss of ^{19}F MRI signal (unpublished data). Even though no crystallization peak was observed in the differential scanning calorimetry (DSC) curves (unpublished data), we hypothesize that the heating and manipulation of the polymer through extruders, followed by cooling on winders, provoke conformational changes in the disposition of the ^{19}F atoms, limiting their movements. To address this problem, further investigations will explore textile fibers composed of a ^{19}F-TPU core and an outer shell consisting of a polymer with excellent spinnability characteristics, such as PVDF or polyethylene terephthalate.

Hybrid ^{1}H/^{19}F MRI is typically susceptible to chemical shift artifacts due to the difference in resonance frequencies between ^{1}H and ^{19}F nuclei, leading to misregistration or misalignment of the images, and signal interference due to the presence of both nuclei in the same region of interest [41,42]. Moreover, the combination with iron-based contrast agents (i.e., SPIONs) can produce artifacts due to magnetic field inhomogeneities and iron susceptibility to magnetic fields, leading to geometric distortions, signal voids, and blooming effects [43]. These artifacts can affect image quality and interpretation, potentially compromising the diagnostic accuracy of MRI scans. Additionally, the lower gyromagnetic ratio and relaxation properties of ^{19}F MRI, which lead to lower sensitivity and thus, longer measurement times, along with the need for custom-built radiofrequency coils tuned to the ^{19}F resonance frequency (40.05 MHz/T), have limited the ^{1}H/^{19}F MRI clinical application to date [19,20]. However, as evidenced by our in vitro and in vivo investigations, the combination of our oleic-acid coated SPIONs with ^{19}F-TPU fibers does not cause any relevant interference or artifacts, highlighting the potential of our approach to foster ^{19}F MRI clinical translation.

In our study, a double-tuned ^{1}H/^{19}F volume coil with limited sensitivity to ^{19}F compared to other coil designs was used. Here improved MRI hardware, pulse sequences, broadband amplifiers, coils, and post-processing and image reconstruction software may help us to reduce the scan time and increase ^{19}F MRI sensitivity in the future. For example, different groups already suggested to modify the quadrature mode of birdcage coils, employing shingled-leg coil design, combining two coils using magnetic coupling, inserting shields and dielectric materials into the coil design, or using PIN-diodes switches [44–47].

[19]F MRI could also be combined with other non-invasive and non-destructive imaging modalities, such as US, positron emission tomography (PET), and single-photon emission computed tomography (SPECT), providing precise quantification, high sensitivity, functional information, low background, and high resolution without expected interference. For example, studies already showed the potential of a hybrid ^{19}F MRI and PET approach for precise and accurate imaging of inflammation, or ^{19}F MRI and SPECT to improve diagnostic accuracy and guided therapy [48,49]. Furthermore, as already published by different groups, the combined application of ^{19}F MRI and US might also provide valuable insights into the integrity or disruption of the vessel endothelial lining, hyperplasia of the intima, development of atherosclerosis and thrombosis by foam cell formation, and acute or chronic inflammation [50–54].

The biocompatibility of our labeled TEVGs was demonstrated in vitro, in vivo, and ex vivo via XTT assay, visual assessment of the post-surgery incisions, and histology results. Despite SPIONs' desirable characteristics, such as biodegradability and tailorable accumulation and retention time, they are known to potentially induce reactive oxygen species (ROS) formation if not coated with biocompatible materials. ROS formation can potentially cause cell-cell signaling interference, gene transcription alteration, necrosis, and apoptosis [55]. Previous studies conducted by our group investigated scaffolds labeled with iron oxide nanoparticles (SPIONs and ultrasmall superparamagnetic iron oxide nanoparticles, USPIOs) via in vivo hybrid positron emission tomography-computed tomography (PET-CT) and ex vivo immunofluorescence analyses showing no in situ inflammation or differences with the unlabeled counterparts [13,56]. Furthermore, in line with previous findings by Rama et al. our follow-up study demonstrates that PLGA fibers labeled with SPIONs, coated with oleic acid to avoid aggregation, toxicity, and immunogenicity, do not elicit an inflammatory reaction upon in vivo implantation [12]. As recently reported, the employment of oleic acid as a coating material of iron nanoparticles protects cells from SPIONs-induced ROS and cell death [57]. Nonetheless, further studies are still required to evaluate long-term SPIONs toxicity toward different cells and tissues and, consequently, identify the most effective strategy to engineer SPIONs' surface and coating [58].

[19]F-labeled polymers or contrast agents are widely investigated as fluorine is chemically inert and, based on current knowledge, non-immunogenic [59,60]. Although fluorine is known to interact with calcium, abundant in bones and teeth, ^{19}F-TPU fibers, not exposed to the lumen of the vascular prostheses, are not expected to undergo significant metabolism and biotransformation. However, the calcification of non-degradable polymers has been described as a significant issue affecting the function and long-term durability of vascular implants [61–63]. Therefore, further studies are deeply needed to investigate the potential calcification within our TEVGs in a longer monitoring period.

Fluorinated surfaces are also well-known for their non-adhesive nature. They possess very low surface energy, which makes them highly hydrophobic and minimizes interactions with polar molecules, including water, proteins, and cells [64,65]. This non-adhesive property

might yield advantages, such as reduced hyperplasia of the intima, risk of blood clot formation, stenosis, thrombosis, and inflammation, as well as negative implications, such as reduced cell-material interactions, which can be detrimental when designing materials for TE. Thus, to avoid hindering cell attachment and growth as well as TEVGs integration within the host organism, we opted to use ^{19}F-TPU fibers as an MRI label instead of producing a textile scaffold completely consisting of ^{19}F-TPU. Furthermore, the chemical, physical, and morphological properties of the TEVGs textile scaffold's surface might also play an important role in cellular response upon implantation. Different studies have extensively explored tailoring polymer characteristics, such as wettability, hydrophobicity, adhesivity, and topography, to influence protein adsorption, cell attachment, function, and matrix formation while also reshaping cytokine profile and immune cell activation, which is pivotal for maintaining a balance between wound healing, tissue regeneration, and implant rejection [8,66]. In this regard, our TEVGs, with and without ^{19}F-TPU fibers, were found to evoke a comparable number of infiltrated immune cells, similar ECM content, and no altered cellular behavior, indicating no cellular toxicity and a comparable immune system response most probably due to balanced wettability, hydrophobicity, adhesivity, and overall biocompatibility of our TEVGs, even with the inclusion of ^{19}F-TPU fibers within the textile scaffold. Nonetheless, further studies are still needed to fully characterize ^{19}F-TPU from a material point of view and functionalize its surface to achieve enhanced biocompatibility via controlled adhesion and specific cell-material or material-material interactions.

5. Conclusions

In this manuscript, we introduce a concept for the complementary non-invasive longitudinal assessment of cardiovascular implants using ^{1}H/^{19}F MRI. Our approach makes TEVGs visible by biocompatible MRI labels, enabling simultaneous monitoring of the degradation and remodeling process while preserving essential information about the positioning and structural integrity. Moreover, we demonstrate the feasibility of imaging TEVGs with an inner diameter of 1.5 mm that can be produced and implanted in the rat abdominal aorta. This highlights that our TEVGs may even be used for small human vessels, such as the coronary arteries. Our approach is applicable in vivo and holds promise for enhancing clinical translation by offering an innovative and specific non-invasive monitoring method for textile scaffolds.

CRediT authorship contribution statement

Elena Rama: Writing – review & editing, Writing – original draft, Visualization, Validation, Methodology, Investigation, Formal analysis, Data curation, Conceptualization. **Saurav Ranjan Mohapatra:** Methodology, Investigation, Conceptualization. **Yukiharu Sugimura:** Methodology, Investigation, Conceptualization. **Tomoyuki Suzuki:** Methodology, Investigation. **Stefan Siebert:** Methodology, Investigation. **Roman Barmin:** Methodology, Investigation, Conceptualization. **Juliane Hermann:** Methodology, Investigation, Data curation. **Jasmin Baier:** Methodology, Investigation. **Anne Rix:** Methodology, Investigation. **Teresa Lemainque:** Methodology, Investigation, Conceptualization. **Susanne Koletnik:** Methodology, Investigation. **Asmaa Said Elshafei:** Methodology, Investigation. **Roger Molto Pallares:** Methodology, Investigation, Conceptualization. **Seyed Mohammadali Dadfar:** Methodology, Investigation. **René H. Tolba:** Project administration. **Volkmar Schulz:** Methodology, Conceptualization. **Joachim Jankowski:** Supervision, Investigation, Data curation. **Christian Apel:** Methodology, Investigation, Conceptualization. **Payam Akhyari:** Supervision, Data curation, Conceptualization. **Stefan Jockenhoevel:** Supervision, Data curation, Conceptualization. **Fabian Kiessling:** Writing – review & editing, Supervision, Project administration, Funding acquisition, Conceptualization.

Declaration of generative AI and AI-assisted technologies in the writing process

During the preparation of this work the author(s) used ChatGPT/OpenAI in order to improve language and readability. After using this tool/service, the author(s) reviewed and edited the content as needed and take(s) full responsibility for the content of the publication.

Declaration of competing interest

The authors declare that they have no known competing financial interests or personal relationships that could have appeared to influence the work reported in this paper.

Data availability

Data will be made available on request.

Acknowledgements

Appendix A. Supplementary data

Supplementary data to this article can be found online at https://doi.org/10.1016/j.biomaterials.2024.122669.

References

[1] G.A. Mensah, G.A. Roth, V. Fuster, The global burden of cardiovascular diseases and risk factors - 2020 and beyond, J. Am. Coll. Cardiol. 74 (2019) 2529–2532, https://doi.org/10.1016/j.jacc.2019.10.009.

[2] C.W. Tsao, A.W. Aday, Z.I. Almarzooq, C.A.M. Anderson, P. Arora, C.L. Avery, C.M. Baker-smith, A.Z. Beaton, A.K. Boehme, A.E. Buxton, Y. Commodore-mensah, M.S.V. Elkind, K.R. Evenson, C. Eze-nliam, S. Fugar, G. Generoso, N.S. Shah, E.L. Thacker, S.S. Virani, Heart disease and stroke statistics — 2023 update : a Report from the American heart association. https://doi.org/10.1161/CIR.0000000000001123, 2023.

[3] L.E. Niklason, J.H. Lawson, Bioengineered Human Blood Vessels, 2020, p. 8682, https://doi.org/10.1126/science.aaw8682.

[4] J.T. Patterson, T. Gilliland, M.W. Maxfield, S. Church, Y. Naito, T. Shinoka, Tissue-engineered vascular grafts for use in the treatment of congenital heart disease : from the bench to the clinic and back again, Futur. Med. (n.d.) 409–419.

[5] C.E.T. Stowell, Y. Wang, Quickening: Translational Design of Resorbable Synthetic Vascular Grafts, 2018, p. 7330.

[6] P. Zilla, M. Deutsch, D. Bezuidenhout, N.H. Davies, T. Pennel, Progressive reinvention or destination lost ? Half a century of cardiovascular tissue engineering, Front. Cardiovasc. Med. 7 (2020) 1–32, https://doi.org/10.3389/fcvm.2020.00159.

[7] J.D. Drews, V.K. Pepper, C.A. Best, J.M. Szafron, J.P. Cheatham, A.R. Yates, K.N. Hor, J.C. Zbinden, Y. Chang, G.J.M. Mirhaidari, A.B. Ramachandra, S. Miyamoto, K.M. Blum, E.A. Onwuka, J. Zakko, J. Kelly, S.L. Cheatham, N. King, J.W. Reinhardt, T. Sugiura, H. Miyachi, Y. Matsuzaki, J. Breuer, E.D. Heuer, T.A. West, T. Shoji, D. Berman, B.A. Boe, J. Asnes, M. Galantowicz, G. Matsumura, N. Hibino, A.L. Marsden, Spontaneous reversal of stenosis in tissue-engineered vascular grafts, Sci. Transl. Med. 12 (2020) 1–14.

[8] F. Zhang, M.W. King, Immunomodulation strategies for the successful regeneration of a tissue-engineered vascular graft, Adv. Healthcare Mater. 11 (2022) 1–24, https://doi.org/10.1002/adhm.202200045.

[9] J.G. Bartolacci, M.N. Behun, J.P. Warunek, T. Li, A. Sahu, G.K. Dwyer, A. Lucas, J. Rong, F. Ambrosio, H.R. Turnquist, S.F. Badylak, Matrix-bound nanovesicle-

associated IL-33 supports functional recovery after skeletal muscle injury by initiating a pro-regenerative macrophage phenotypic transition, Npj Regen. Med. 9 (2024), https://doi.org/10.1038/s41536-024-00346-2.

[10] U. Jehn, K. Schuette-nuetgen, D. Kentrup, V. Hoerr, S. Reuter, Renal allograft rejection : noninvasive ultrasound- and MRI-based diagnostics, Contrast Media Mol. Imaging 2019 (2019).

[11] Kilian M.A. Mueller, Geoffrey J. Topping, Sebastian P. Schwaminger, Younzhe Zou, Diana M. Rojas-Gonzalez, Elena M. De-Juan-Pardo, Sonja Berensmeier, Franz Schilling, Petra Mela, Visualization of USPIO-labeled melt-electrowritten scaffolds by non-invasive magnetic resonance imaging, Biomater. Sci. (2021) 4607–4612, https://doi.org/10.1039/d1bm00461a.

[12] E. Rama, S.R. Mohapatra, C. Melcher, T. Nolte, S.M. Dadfar, R. Brueck, V. Pathak, A. Rix, T. Gries, V. Schulz, T. Lammers, C. Apel, S. Jockenhoevel, F. Kiessling, Monitoring the remodeling of biohybrid tissue-engineered vascular grafts by multimodal molecular imaging, Adv. Sci. 9 (2022) 1–15, https://doi.org/10.1002/advs.202105783.

[13] F. Wolf, V. Paefgen, O. Winz, M. Mertens, S. Koch, N. Gross-Weege, A. Morgenroth, A. Rix, H. Schnoering, K. Chalabi, S. Jockenhoevel, T. Lammers, F. Mottaghy, F. Kiessling, P. Mela, MR and PET-CT monitoring of tissue-engineered vascular grafts in the ovine carotid artery, Biomaterials 216 (2019) 119228, https://doi.org/10.1016/j.biomaterials.2019.119228.

[14] R. Garnett, A comprehensive review of dual-energy and multi-spectral computed tomography, Clin. Imag. 67 (2020) 160–169, https://doi.org/10.1016/j.clinimag.2020.07.030.

[15] K. Rajendran, M. Petersilka, A. Henning, E.R. Shanblatt, B. Schmidt, T.G. Flohr, A. Ferrero, F. Baffour, F.E. Diehn, L. Yu, P. Rajiah, J.G. Fletcher, S. Leng, C. H. McCollough, First clinical photon-counting detector CT system: technical evaluation, Radiology 303 (2022) 130–138, https://doi.org/10.1148/RADIOL.212579.

[16] Y. Xiao, R. Paudel, J. Liu, C. Ma, Z. Zhang, S. Zhou, Int. J. Mol. Med. (2016) 1319–1326, https://doi.org/10.3892/ijmm.2016.2744. MRI contrast agents: Classification and application (Review).

[17] M. Jeon, M.V. Halbert, Z.R. Stephen, M. Zhang, Iron oxide nanoparticles as T1 contrast agents for magnetic resonance imaging: fundamentals, challenges, applications, and prospectives, Adv. Mater. 33 (2021) 1–18, https://doi.org/10.1002/adma.201906539.

[18] T. Shin, J. Choi, S. Yun, I. Kim, H. Song, Y. Kim, K. In Park, J. Cheon, T1 and T2 dual-mode MRI contrast agent for enhancing accuracy by engineered nanomaterials, ACS Nano (2014) 3393–3401.

[19] I. Tirotta, V. Dichiarante, C. Pigliacelli, G. Cavallo, G. Terraneo, F.B. Bombelli, P. Metrangolo, G. Resnati, 19F magnetic resonance imaging (MRI): from design of materials to clinical applications, Chem. Rev. 115 (2015) 1106–1129, https://doi.org/10.1021/cr500286d.

[20] C. Zhang, S.S. Moonshi, Y. Han, S. Puttick, H. Peng, B.J.A. Magoling, J.C. Reid, S. Bernardi, D.J. Searles, P. Král, A.K. Whittaker, PFPE-based polymeric 19F MRI agents: a new class of contrast agents with outstanding sensitivity, Macromolecules 50 (2017) 5953–5963, https://doi.org/10.1021/acs.macromol.7b01285.

[21] T. Lammers, M.E. Mertens, P. Schuster, K. Rahimi, V. Schulz, A.J.C. Kuehne, S. Jockenhoevel, F. Kiessling, Fluorinated polyurethane scaffolds for 19F magnetic resonance imaging, Chem. Mater. 29 (2017) 2669–2671, https://doi.org/10.1021/acs.chemmater.6b04649.

[22] S.R. Mohapatra, E. Rama, C. Melcher, T. Call, M.A. Al Enezy-Ulbrich, A. Pich, C. Apel, F. Kiessling, S. Jockenhoevel, From in vitro to perioperative vascular tissue engineering: shortening production time by traceable textile-reinforcement, Tissue Eng. Regen. Med. 19 (2022) 1169–1184, https://doi.org/10.1007/s13770-022-00482-0.

[23] M. Patel, A. Jha, R. Patel, Potential application of PLGA microsphere for tissue engineering, J. Polym. Res. 28 (2021), https://doi.org/10.1007/s10965-021-02562-6.

[24] S. Mohammadali, K. Roemhild, N.I. Drude, S. Von Stillfried, R. Knüchel, F. Kiessling, T. Lammers, Iron Oxide Nanoparticles : Diagnostic , Therapeutic and Theranostic Applications, 138, 2019, pp. 302–325, https://doi.org/10.1016/j.addr.2019.01.005.

[25] R. Hufschmid, H. Arami, R.M. Ferguson, M. Gonzales, E. Teeman, L.N. Brush, D. Browning, K.M. Krishnan, Synthesis of phase-pure and monodisperse ironoxide nanoparticles by thermal decomposition, Nanoscale (2015) 11142–11154, https://doi.org/10.1039/c5nr01651g.

[26] R.G. Marangoni, B. Korman, J. Varga, Adipocytic progenitor cells give rise to pathogenic myofibroblasts: adipocyte-to-mesenchymal transition and its emerging role in fibrosis in multiple organs, Curr. Rheumatol. Rep. 22 (2020), https://doi.org/10.1007/s11926-020-00957-w.

[27] S. Lin, K. Mequanint, Bioreactor-induced mesenchymal progenitor cell differentiation and elastic fiber assembly in engineered vascular tissues, Acta Biomater. 59 (2017) 200–209, https://doi.org/10.1016/j.actbio.2017.07.012.

[28] A.J. Collins, R.N. Foley, D.T. Gilbertson, S.C. Chen, United States Renal Data System public health surveillance of chronic kidney disease and end-stage renal disease, Kidney Int. Suppl. 5 (2015) 2–7, https://doi.org/10.1038/kisup.2015.2.

[29] A.F. Schild, E. Perez, E. Gillaspie, C. Seaver, J. Livingstone, A. Thibonnier, Arteriovenous fistulae vs. arteriovenous grafts: a retrospective review of 1,700 consecutive vascular access cases, J. Vasc. Access 9 (2008) 231–235, https://doi.org/10.1177/112972980800900402.

[30] R.L. Madden, G.S. Lipkowitz, B.J. Browne, A. Kurbanov, A comparison of cryopreserved vein allografts and prosthetic grafts for hemodialysis access, Ann. Vasc. Surg. 19 (2005) 686–691, https://doi.org/10.1007/s10016-005-6621-2.

[31] S.L.M. Dahl, A.P. Kypson, J.H. Lawson, J.L. Blum, J.T. Strader, Y. Li, R.J. Manson, W.E. Tente, L. DiBernardo, M.T. Hensley, R. Carter, T.P. Williams, H.L. Prichard,

M.S. Dey, K.G. Begelman, L.E. Niklason, Readily available tissue-engineered vascular grafts, Sci. Transl. Med. 3 (2011), https://doi.org/10.1126/scitranslmed.3001426.

[32] T.S. Hirotsugu Kurobe, Mark W. Maxfield, Christopher K. Breuer, Concise review: tissue-engineered vascular grafts for cardiac surgery: past, present, and future, Stem Cells Transl. Med. 1 (2012) 566–571.

[33] B. Brandstrup, Fluid therapy for the surgical patient, Best Pract. Res. Clin. Anaesthesiol. 20 (2006) 265–283, https://doi.org/10.1016/j.bpa.2005.10.007.

[34] S. Cho, D.E. Discher, K.W. Leong, G. Vunjak-Novakovic, J.C. Wu, Challenges and opportunities for the next generation of cardiovascular tissue engineering, Nat. Methods 19 (2022) 1064–1071, https://doi.org/10.1038/s41592-022-01591-3.

[35] R.Z. Zhuang, R. Lock, B. Liu, G. Vunjak-Novakovic, Opportunities and challenges in cardiac tissue engineering from an analysis of two decades of advances, Nat. Biomed. Eng. 6 (2022) 327–338, https://doi.org/10.1038/s41551-022-00885-3.

[36] D. Kim, J.J. Chung, Y. Jung, S.H. Kim, The effect of Substance P/Heparin conjugated PLCL polymer coating of bioinert ePTFE vascular grafts on the recruitment of both ECs and SMCs for accelerated regeneration, Sci. Rep. (2019) 1–13, https://doi.org/10.1038/s41598-019-53514-6.

[37] Z. Zhu, H. Gu, H. Zhang, H. Wang, H. Xia, X. Mo, J. Wu, Covalent grafting of PEG and heparin improves biological performance of electrospun vascular grafts for carotid artery replacement, Acta Biomater. 119 (2021) 211–224, https://doi.org/10.1016/j.actbio.2020.11.013.

[38] T.W. Hatem Jouda, Luis larrea murillo, clinical applications, Cells 11 (2022) 445–456.

[39] A. Porzionato, E. Stocco, S. Barbon, F. Grandi, V. Macchi, R. De Caro, Tissue-engineered grafts from human decellularized extracellular matrices: a systematic review and future perspectives, Int. J. Mol. Sci. 19 (2018), https://doi.org/10.3390/ijms19124117.

[40] X. Zhang, X. Chen, H. Hong, R. Hu, J. Liu, C. Liu, Decellularized extracellular matrix scaffolds: recent trends and emerging strategies in tissue engineering, Bioact, Mater 10 (2022) 15–31, https://doi.org/10.1016/j.bioactmat.2021.09.014.

[41] L. Wu, F. Liu, S. Liu, X. Xu, Z. Liu, X. Sun, Perfluorocarbons-based 19F magnetic resonance imaging in biomedicine, Int. J. Nanomed. 15 (2020) 7377–7395, https://doi.org/10.2147/IJN.S255084.

[42] C.H. Choi, S.M. Hong, J. Felder, N.J. Shah, The state-of-the-art and emerging design approaches of double-tuned RF coils for X-nuclei, brain MR imaging and spectroscopy: a review, Magn. Reson. Imaging 72 (2020) 103–116, https://doi.org/10.1016/j.mri.2020.07.003.

[43] A. Hahn, F.T. Kurz, Advanced Imaging/MRI for Tissue Engineering, third ed., Elsevier Ltd., 2021 https://doi.org/10.1016/B978-0-12-820508-2.00016-7.

[44] P. Bowyer, J. Finnigan, B. Marsden, B. Taber, A. Zens, Using magnetic coupling to implement 1H, 19F, 13C experiments in routine high resolution NMR probes, J. Magn. Reson. 261 (2015) 190–198, https://doi.org/10.1016/j.jmr.2015.10.010.

[45] S. Ha, M.J. Hamamura, O. Nalcioglu, L.T. Muftuler, A PIN diode controlled dual-tuned MRI RF coil and phased array for multi nuclear imaging, Phys. Med. Biol. 55 (2010) 2589–2600, https://doi.org/10.1088/0031-9155/55/9/011.

[46] L. Hu, F.D. Hockett, J. Chen, L. Zhang, S.D. Caruthers, G.M. Lanza, S.A. Wickline, A generalized strategy for designing 19F/1H dual-frequency MRI coil for small animal imaging at 4.7 Tesla, J. Magn. Reson. Imag. 34 (2011) 245–252, https://doi.org/10.1002/jmri.22516.

[47] P. Villa-Valverde, I. Rodríguez, D. Padró, M. Benito, C.E. Garrido-Salmon, J. Ruiz-Cabello, A dual 1 H/19 F birdcage coil for small animals at 7 T MRI, Magn. Reson. Mater. Physics, Biol. Med. 32 (2019) 79–87, https://doi.org/10.1007/s10334-018-00733-z.

[48] Z. Guo, M. Chen, C. Peng, S. Mo, C. Shi, G. Fu, X. Wen, R. Zhuang, X. Su, T. Liu, N. Zheng, X. Zhang, pH-sensitive radiolabeled and superfluorinated ultra-small palladium nanosheet as a high-performance multimodal platform for tumor theranostics, Biomaterials 179 (2018) 134–143, https://doi.org/10.1016/j.biomaterials.2018.06.040.

[49] C. Wang, B.I. Leach, D. Lister, S.R. Adams, H. Xu, C. Hoh, P. McConville, J. Zhang, K. Messer, E.T. Ahrens, Metallofluorocarbon nanoemulsion for inflammatory macrophage detection via PET and MRI, J. Nucl. Med. 62 (2021) 1146–1153, https://doi.org/10.2967/JNUMED.120.255273.

[50] A. Dasgupta, M. Liu, T. Ojha, G. Storm, F. Kiessling, T. Lammers, Ultrasound-mediated drug delivery to the brain: principles, progress and prospects, Drug Discov. Today Technol. 20 (2016) 41–48, https://doi.org/10.1016/j.ddtec.2016.07.007.

[51] D. Janasik, T. Krawczyk, 19F MRI probes for multimodal imaging, Chem. Eur J. 28 (2022), https://doi.org/10.1002/chem.202102556.

[52] R. Díaz-López, N. Tsapis, E. Fattal, Liquid perfluorocarbons as contrast agents for ultrasonography and 19F-MRI, Pharm. Res. (N. Y.) 27 (2010) 1–16, https://doi.org/10.1007/s11095-009-0001-5.

[53] A. Curaj, Z. Wu, S. Fokong, E.A. Liehn, C. Weber, A. Burlacu, T. Lammers, M. Van Zandvoort, F. Kiessling, Noninvasive molecular ultrasound monitoring of vessel healing after intravascular surgical procedures in a preclinical setup, Arterioscler. Thromb. Vasc. Biol. 35 (2015) 1366–1373, https://doi.org/10.1161/ATVBAHA.114.304857.

[54] A. Curaj, Z. Wu, A. Rix, O. Gresch, M. Sternkopf, S. Alampour-Rajabi, T. Lammers, M. Van Zandvoort, C. Weber, R.R. Koenen, E.A. Liehn, F. Kiessling, Molecular ultrasound imaging of junctional adhesion molecule A depicts acute alterations in blood flow and early endothelial dysregulation, Arterioscler. Thromb. Vasc. Biol. 38 (2018) 40–48, https://doi.org/10.1161/ATVBAHA.117.309503.

[55] V. Frantellizzi, M. Conte, M. Pontico, A. Pani, R. Pani, G. De Vincentis, New frontiers in molecular imaging with superparamagnetic iron oxide nanoparticles (SPIONs): efficacy, toxicity, and future applications, Nucl. Med. Mol. Imaging 54 (2010) 65–80, https://doi.org/10.1007/s13139-020-00635-w, 2020.

[56] M.E. Mertens, A. Hermann, A. Bühren, L. Olde-Damink, D. Möckel, F. Gremse, J. Ehling, F. Kiessling, T. Lammers, Iron oxide-labeled collagen scaffolds for non-invasive MR imaging in tissue engineering, Adv. Funct. Mater. 24 (2014) 754–762, https://doi.org/10.1002/adfm.201301275.

[57] N. Repar, E.J. Jovičić, A. Kump, G. Birarda, L. Vaccari, A. Erman, S. Kralj, S. Nemec, T. Petan, D. Drobne, Oleic acid protects endothelial cells from silica-coated superparamagnetic iron oxide nanoparticles (SPIONs)-Induced oxidative stress and cell death, Int. J. Mol. Sci. 23 (2022), https://doi.org/10.3390/ijms23136972.

[58] R. Vakili-Ghartavol, A.A. Momtazi-Borojeni, Z. Vakili-Ghartavol, H.T. Aiyelabegan, M.R. Jaafari, S.M. Rezayat, S. Arbabi Bidgoli, Toxicity assessment of superparamagnetic iron oxide nanoparticles in different tissues, Artif. Cells, Nanomedicine Biotechnol. 48 (2020) 443–451, https://doi.org/10.1080/21691401.2019.1709855.

[59] A. Mali, E.L. Kaijzel, H.J. Lamb, L.J. Cruz, 19F-nanoparticles: platform for in vivo delivery of fluorinated biomaterials for 19F-MRI, J. Contr. Release 338 (2021) 870–889, https://doi.org/10.1016/j.jconrel.2021.09.001.

[60] R. Holman, O. Lorton, P.C. Guillemin, S. Desgranges, C. Contino-Pépin, R. Salomir, Perfluorocarbon emulsion contrast agents: a mini review, Front. Chem. 9 (2022) 1–9, https://doi.org/10.3389/fchem.2021.810029.

[61] A. Lejay, B. Bratu, S. Kuntz, N. Neumann, F. Heim, N. Chakfé, Calcification of synthetic vascular grafts: a systematic review, EJVES Vasc. Forum. 60 (2023) 1–7, https://doi.org/10.1016/j.ejvsvf.2023.05.013.

[62] Y. Hayabuchi, K. Mori, T. Kitagawa, M. Sakata, S. Kagami, Polytetrafluoroethylene graft calcification in patients with surgically repaired congenital heart disease: evaluation using multidetector-row computed tomography, Am. Heart J. 153 (2007) 806.e1–806.e8, https://doi.org/10.1016/j.ahj.2007.01.035.

[63] A.A. Gostev, V.S. Chernonosova, I.S. Murashov, D.S. Sergeevichev, A. A. Korobeinikov, A.M. Karaskov, A.A. Karpenko, P.P. Laktionov, Electrospun polyurethane-based vascular grafts: physicochemical properties and functioning in vivo, Biomed. Mater. 15 (2020), https://doi.org/10.1088/1748-605X/ab550c.

[64] D.W. Grainger, C.W. Stewart, Fluorinatecl coatings and films: motivation and significance, ACS Symp. Ser. 787 (2001) 1–14, https://doi.org/10.1021/bk-2001-0787.ch001.

[65] H. Peng, I. Blakey, B. Dargaville, F. Rasoul, S. Rose, A.K. Whittaker, Synthesis and evaluation of partly fluorinated block copolymers as MRI imaging agents, Biomacromolecules 10 (2009) 374–381, https://doi.org/10.1021/bm801136m.

[66] S. Franz, S. Rammelt, D. Scharnweber, J.C. Simon, Immune responses to implants - a review of the implications for the design of immunomodulatory biomaterials, Biomaterials 32 (2011) 6692–6709, https://doi.org/10.1016/j.biomaterials.2011.05.078.